MEASUREMENT OF ELECTROMAGNETIC PROPERTIES
OF LIGHTNING WITH 10 NANOSECOND RESOLUTION

C. E. Baum, E. L. Breen, and J. P. O'Neill
Air Force Weapons Laboratory

C. B. Moore and D. L. Hall
New Mexico Institute of Mining and Technology

ABSTRACT

This paper presents electromagnetic data recorded from lightning strikes.
The data analysis reveals general characteristics of fast electromagnetic fields
measured at the ground including rise times, amplitudes, and time patterns. A
look at the electromagnetic structure of lightning shows that the shortest rise
times in the vicinity of 30 ns are associated with leader streamers. Lightning
location is based on electromagnetic field characteristics and is compared to
a nearby sky camera. The fields from both leaders and return strokes have been
measured and are discussed.

The data were obtained during 1978 and 1979 from lightning strikes occur-
ring within 5 kilometers of an underground metal instrumentation room located
on South Baldy peak near Langmuir Laboratory, New Mexico. The computer con-
trolled instrumentation consisted of sensors previously used for measuring the
nuclear electromagnetic pulse (EMP) and analog-digital recorders with 10 ns
sampling, 256 levels of resolution, and 2 kilobytes of internal memory.

I. INTRODUCTION

In the summers of 1978 and 1979 a set of measurements of the electromag-
netic fields from natural lightning was made near the top of South Baldy peak
(elevation 3275 m) which also houses Langmuir Laboratory near Socorro, New
Mexico, U.S.A. As will be discussed in this paper the data consist of time
waveforms of about 20 µs duration at a 10 ns sample spacing for the three elec-
tromagnetic field components (one electric and two magnetic) which exist
adjacent to a conducting ground plane on top of the "iron Kiva" (or Kiva) (our
screen room buried in the top of the mountain) and the surrounding earth surface
(see fig. 1.1). The details of the instrumentation system are discussed in
another paper (ref. 5).

As background, these measurements resulted from some interest in the dif-
ference between lightning and the nuclear electromagnetic pulse. For nuclear
detection purposes it is desirable to reliably detect a nuclear EMP event
without false triggering by lightning. The ARGUS-1A detector system was
designed with the high altitude EMP environment in mind (ref. 2). For this

purpose magnetic (loop) sensors were used to avoid the low-frequency electric field from lightning and local static charging effects. In addition the sensors respond to the derivative of the field to emphasize the high frequencies present in the high-altitude nuclear EMP. Essentially one is looking for a pulse with 10 ns to 100 ns important characteristic times.

In order to understand the sensitivity of the ARGUS-1A to lightning two things were done. First the detectors were placed on South Baldy peak and their response to lightning monitored. Second, and more important for this paper, the fast transient characteristics of the transient electromagnetic fields (in time-derivative form) were measured. It is these measurements and some analysis of them which are presented here.

The field sensors consist of two MGL-3 B-dot sensors and one ACD-5 D-dot sensor located on the roof (ground plane) of a buried shield enclosure (Kiva). The roof of the Kiva is flush with the earth surface and is electrically connected to the center of a 30 m × 30 m wire-mesh ground plane. Data recording is accomplished by Biomation 8100 waveform recorders controlled by an HP 9825 calculator. A more complete description of the instrumentation is presented in reference 5.

At first we had little idea of what to expect. We made some measurements (section 2) which showed us some of the signal levels and patterns in the waveforms of the field time derivatives, and in the time integral of these waveforms. Based on the kinds of pulses observed and their time patterns it appeared that these related to individual fast pulses along some leader formation process. This led to a model (section 3) which with ranging information (section 4) allowed us to infer some of the characteristics of the current in the lightning streamer. Section 5 then applies this to some of the data obtained.

II. GENERAL CHARACTERISTICS OF OBSERVED ELECTROMAGNETIC FIELDS

With the instrumentation at the Kiva discussed in reference 5 measurements were begun in the summer of 1978. For use in our data analysis the $\partial \vec{B}/\partial t$ sensors (MGL-3) had $A_{h_{eq}} = 0.1 \ m^2$, and the $\partial \vec{D}/\partial t$ sensor (ACD-5) had $A_{e_{eq}} = 1.0 \ m^2$ for use in the formulas

$$V_h = \vec{A}_{h_{eq}} \cdot \frac{\partial}{\partial t} \vec{B} \quad \text{(open circuit voltage)}$$

$$(2.1)$$

$$I_e = \vec{A}_{e_{eq}} \cdot \frac{\partial}{\partial t} \vec{D} \quad \text{(short circuit current)}$$

where the fields are those in the presence of the ground plane (i.e., including reflection). The response times (10-90 rise times of integrated output for step-function exciting field) into 50 Ω loads are short compared to our 10 ns sampling resolution and hence neglected.

The three sensors responded to the north and east components of $\partial \vec{B}/\partial t$ and to the vertical (up) component of $\partial \vec{D}/\partial t$. The signal from $\partial \vec{B}/\partial t$ north was attenuated a factor of 2 by a power splitter used to send this signal to an additional recorder for other purposes. These corrections and the equivalent areas are all removed for the displays of $\partial \vec{B}/\partial t$ and $\partial \vec{D}/\partial t$ in this paper. The $\vec{B}$ and $\vec{D}$ waveforms are determined by numerical integration of the digital data provided by the Biomation 8100 waveform recorders. Note that the integrated waveforms exhibit baseline slope which is at least partly due to errors in determining the baseline values for the original waveforms; this baseline shift is partly removed by estimating the baseline position near the beginning of the recording. The long-time variation of the integrated waveforms should not be trusted, nevertheless; the purpose of the integration is to see the shape and amplitude of the fast pulses which are more reliable.

A nice property of the Biomation 8100 waveform recorder is that one has a significant length of recording time before the pulse which triggers the system is recorded. This pretrigger data time was set at about 4 µs. The self trigger was used on all three channels with the first trigger level being exceeded triggering all the recorders. Triggering in this case means freezing the data stream and transferring the 20 µs of information to magnetic disk.

Since the recording is digital there is also some limitation in the signal amplitude (voltage) resolution. The full scale is 256 uniformly spaced levels with zero approximately centered. Typical signals deviated about one third from baseline (zero) to the full level on one side of zero.

For some preliminary information let us now consider two examples of the kinds of waveforms we have seen. Detailed analysis of such waveforms is considered in section 5. A representative example of a leader waveform is given in figures 2.1 and 2.2. A representative example of a return-stroke waveform is given in figures 2.3 and 2.4. In both cases only the east components of $\partial \vec{B}/\partial t$ and of $\vec{B}$ are exhibited.

Consider the leader waveform in figure 2.1. Note the complex structure with many individual pulses indicating the progression of the leader as a sequence of impulsive events. The horizontal distance (by flash to bang) to this stroke was about 350 m.

Note the large pulse at about 4 µs which triggered the recording. The first 7 µs of the record is expanded in figure 2.2. From a printout of the digital data this pulse has the approximate characteristics:

pulse at 4.0 µs

$$\frac{\partial}{\partial t} B_E \begin{cases} \text{peak} \simeq 2.42 \text{ T/s} \\ \text{zero to peak rise} \simeq 90 \text{ ns} \\ \text{10-90 rise} \simeq 50 \text{ ns} \end{cases}$$

$$(2.2)$$

$$B_E \begin{cases} \text{baseline to peak} \simeq 0.169 \ \mu T \\ \text{baseline to peak rise} \simeq 150 \ \text{ns} \\ 10\text{-}90 \ \text{rise} \simeq 80 \ \text{ns} \\ \text{width} \simeq 500 \ \text{ns} \end{cases}$$

$$\tau \simeq 70 \ \text{ns}$$

Here τ has been defined as a characteristic time for the rise portion of the waveform with the formula

$$\tau \equiv \frac{\text{waveform peak}}{\text{derivative waveform peak}} \qquad (2.3)$$

Selecting a few more pulses from this waveform for comparison we have

pulse at 1.3 μs

$$\frac{\partial}{\partial t} B_E \begin{cases} \text{peak} \simeq 1.48 \ \text{T/s} \\ \text{zero to peak rise} \simeq 50 \ \text{ns} \\ 10\text{-}90 \ \text{rise} \simeq 30 \ \text{ns} \end{cases}$$

$$(2.4)$$

$$B_E \begin{cases} \text{baseline to peak} \simeq .079 \ \mu T \\ \text{baseline to peak rise} \simeq 100 \ \text{ns} \\ 10\text{-}90 \ \text{rise} \simeq 60 \ \text{ns} \\ \text{width} \simeq 250 \ \text{ns} \end{cases}$$

$$\tau \simeq 53 \ \text{ns}$$

and another

pulse at 12.9 μs

$$\frac{\partial}{\partial t} B_E \begin{cases} \text{peak} \simeq -.86 \ \text{T/s} \\ \text{zero to peak rise} \simeq 60 \ \text{ns} \\ 10\text{-}90 \ \text{rise} \simeq 30 \ \text{ns} \end{cases}$$

$$(2.5)$$

$$
B_E \begin{cases} \text{baseline to peak} \simeq -.03 \ \mu T \\ \text{baseline to peak rise} \simeq 80 \ ns \\ \text{10--90 rise} \simeq 40 \ ns \\ \text{width} \simeq 160 \ ns \end{cases}
$$

$$\tau \simeq 35 \ ns$$

and another

pulse at 14.0 μs

$$
\frac{\partial}{\partial t} B_E \begin{cases} \text{peak} \simeq -.547 \ T/s \\ \text{zero to peak rise} \simeq 40 \ ns \\ \text{10--90 rise} \simeq 30 \ ns \end{cases}
$$

$$
B_E \begin{cases} \text{baseline to peak} \simeq -.014 \ \mu T \\ \text{baseline to peak rise} \simeq 50 \ ns \\ \text{10--90 rise} \simeq 35 \ ns \\ \text{width} \simeq 70 \ ns \end{cases}
$$

(2.6)

$$\tau \simeq 26 \ ns$$

Comparing these individual pulses we have seen characteristic times for the rise ranging from about 70 ns to less than 30 ns. Also one can note that there seems to be a general trend in that smaller pulses have shorter characteristic times for the rise and shorter pulse widths. Pulse widths vary from about 500 ns to about 70 ns.

Now consider the return-stroke waveform in figure 2.3. The $\partial \vec{B}/\partial t$ structure is somewhat simplified by comparison to the previous leader example. The horizontal distance (by flash to bang) to this stroke was about 850 m. Comparing the peak derivative signals between return stroke (fig. 2.3) and leader (fig. 2.1) note that they are of comparable magnitude. Assuming that the leader is elevated somewhat above the ground, the inferred slant ranges to the sources for the two examples are crudely of the same order as well. It therefore seems that we may typically expect peak derivative waveforms from the larger leader pulses to have about the same strength as those for return strokes (at comparable distances).

The main pulse at about 4 μs which triggered the recording is expanded in figure 2.4 for the first 7 μs. Note the wide pulse characteristic of the return stroke as indicated in the east component of the $\vec{B}$ waveform. From a

printout of the digital data this pulse has the approximate characteristics:

pulse at 4.0 μs

$$\frac{\partial}{\partial t} B_E \begin{cases} \text{peak} \simeq -2.81 \text{ T/s} \\ \text{zero to peak rise} \simeq 110 \text{ ns} \\ \text{10-90 rise} \simeq 35 \text{ ns} \end{cases}$$

$$B_E \begin{cases} \text{baseline to peak} \simeq -.129 \text{ μT} \\ \text{baseline to peak rise} \simeq 160 \text{ ns} \\ \text{10-90 rise} \simeq 60 \text{ ns} \\ \text{width} \simeq 1000 \text{ ns} \end{cases}$$

(2.7)

$$\tau \simeq 46 \text{ ns}$$

It does seem that return strokes can be somewhat fast. We have looked at other return strokes and noticed similarly small values of τ. For this type of pulse of $\vec{B}$ the concept of width is somewhat problematical because of the current that continues in the arc after the fast part of the pulse has occurred.

III. FAST TRANSIENT ELECTROMAGNETIC FIELDS AT EARTH SURFACE RELATED TO INDIVIDUAL LIGHTNING CURRENT PULSES

Having seen some of the transient waveforms in section 2, and noting that many of the individual pulses are extremely fast with rise times of the order of some tens of ns, it appeared that one might be able to model these pulses as events somewhat localized in space. This concept uses the limitation of the speed of light on current propagation as compared to the distances of hundreds to thousands of meters from source to observer. As will appear later, this approach yields some valuable insight into the lightning streamer currents and propagation.

Let us begin by defining a spherical (r,θ,ϕ) coordinate system based on the Kiva as in figure 3.1A. For our purposes (r,θ,ϕ) signifies some position in space which is the source of the observed lightning signals at (near) $\vec{r} = \vec{0}$ (the Kiva). In addition to the spherical coordinates we have cylindrical (Ψ,ϕ,z) and cartesian (x,y,z) coordinates all related via

$$x = \Psi \cos(\phi) = r \sin(\theta) \cos(\phi)$$

$$y = \Psi \sin(\phi) = r \sin(\theta) \sin(\phi)$$

$$z = r \cos(\theta)$$

(3.1)

44

$$r^2 = \psi^2 + z^2$$

$$\psi^2 = x^2 + y^2$$

$$\frac{\sin(\phi)}{y} = \frac{\cos(\phi)}{x}$$

with x and y taking the signs of $\cos(\phi)$ and $\sin(\phi)$ respectively. As indicated in figure 3.1A the coordinate system is oriented so that

> x is north (geographical)
>
> y is west
>
> z is up (3.2)
>
> θ is zenith angle
>
> ϕ is counterclockwise from north

Associated with these coordinate sets there are sets of unit vectors (right-handed) as

$$\vec{1}_x \times \vec{1}_y = \vec{1}_z \, , \ \vec{1}_y \times \vec{1}_z = \vec{1}_x \, , \ \vec{1}_z \times \vec{1}_x = \vec{1}_y$$

$$\vec{1}_\psi \times \vec{1}_\phi = \vec{1}_z \, , \ \vec{1}_\phi \times \vec{1}_z = \vec{1}_\psi \, , \ \vec{1}_z \times \vec{1}_\psi = \vec{1}_\phi \qquad (3.3)$$

$$\vec{1}_r \times \vec{1}_\theta = \vec{1}_\phi \, , \ \vec{1}_\theta \times \vec{1}_\phi = \vec{1}_r \, , \ \vec{1}_\phi \times \vec{1}_r = \vec{1}_\theta$$

which are related by

$$\vec{1}_\psi = \vec{1}_x \cos(\phi) + \vec{1}_y \sin(\phi)$$

$$\vec{1}_\phi = -\vec{1}_x \sin(\phi) + \vec{1}_y \cos(\phi)$$

$$\qquad (3.4)$$

$$\vec{1}_r = \vec{1}_\psi \sin(\theta) + \vec{1}_z \cos(\theta)$$

$$\vec{1}_\theta = \vec{1}_\psi \cos(\theta) - \vec{1}_z \sin(\theta)$$

In addition to the coordinates for the source point with respect to the observation point let us define a set of unit vectors for describing the wave propagation to the observer. These are a right-handed system

$$\vec{1}_1 \times \vec{1}_2 = \vec{1}_3 \, , \ \vec{1}_2 \times \vec{1}_3 = \vec{1}_1 \, , \ \vec{1}_3 \times \vec{1}_1 = \vec{1}_2 \qquad (3.5)$$

which are related to our previously defined coordinate unit vectors as

$$\vec{1}_1 \equiv -\vec{1}_r$$

$$\vec{1}_2 \equiv -\vec{1}_\phi \tag{3.6}$$

$$\vec{1}_3 \equiv -\vec{1}_\theta$$

Viewed from an observer at the Kiva one has the picture in figure 3.1B in which

$$\vec{1}_1 \equiv \text{direction of propagation}$$
$$\equiv \text{pointing to observer}$$

$$\vec{1}_2 \equiv \text{horizontal to right} \tag{3.7}$$

$$\vec{1}_3 \equiv \text{"up" as modified by being perpendicular to } \vec{1}_1$$

Note that $\vec{1}_2$ and $\vec{1}_3$ are polarization vectors for the wave. The plane of incidence is defined by $\vec{r}$ and the z axis; it contains $\vec{1}_1$ and $\vec{1}_3$ as well as $\vec{1}_r$, $\vec{1}_\theta$, $\vec{1}_\psi$, and $\vec{1}_z$; $\vec{1}_2$ and $\vec{1}_\theta$ are perpendicular to the plane of incidence.

Next consider some distribution of current density $\vec{J}(\vec{r},t)$ in free space. The electromagnetic fields from this can be represented as (ref. 1)

$$\tilde{\vec{E}}_{inc}(\vec{r}',s) = -\left\langle \tilde{\overleftrightarrow{Z}}(\vec{r}',\vec{r}'';s) \; ; \; \tilde{\vec{J}}(\vec{r}'',s) \right\rangle$$

$$\tilde{\vec{H}}_{inc}(\vec{r}',s) = \frac{1}{s\mu_o} \left\langle \nabla \times \tilde{\overleftrightarrow{Z}}(\vec{r}',\vec{r}'';s) \; ; \; \tilde{\vec{J}}(\vec{r}'',s) \right\rangle \tag{3.8}$$

with the subscript inc indicating incident at the observer at $\vec{r}' = \vec{0}$ and where $\vec{r}', \vec{r}''$ are now general coordinates (positions), s is the Laplace-transform variable (or complex frequency) with respect to time t (in general two sided) and the tilde ~ indicates a Laplace-transformed quantity. The impedance kernel is

$$\tilde{\overleftrightarrow{Z}}(\vec{r}',\vec{r}'';s) = s\mu_o \tilde{\overleftrightarrow{G}}_o(\vec{r}',\vec{r}'';s)$$

$$\tilde{\overleftrightarrow{G}}_o(\vec{r}',\vec{r}'';s) = \left[\overleftrightarrow{1} - \gamma^{-2}\nabla'\nabla'\right] \tilde{G}_o(\vec{r}',\vec{r}'';s)$$

$$\equiv \text{dyadic Green's function of free space}$$

$$\tilde{G}_o = \gamma \frac{e^{-\zeta}}{4\pi\zeta} \quad (\text{for } \vec{r}' \neq \vec{r}'') \tag{3.9}$$

$$\equiv \text{scalar Green's function of free space}$$

$$\gamma \equiv \frac{s}{c} \equiv \text{free space propagation constant}$$

$$c \equiv \frac{1}{\sqrt{\mu_o \varepsilon_o}} \simeq 3 \times 10^8 \text{ m/s}$$

$\equiv$ speed of light (in free space)

$$Z_o \equiv \sqrt{\frac{\mu_o}{\varepsilon_o}} \simeq 377 \ \Omega$$

$\equiv$ wave impedance of free space

$$\zeta \equiv \gamma |\vec{r}' - \vec{r}''|$$

The symbol $<,>$ indicates integration over the space coordinates common to the two terms (r'' in (3.8)). The free-space dyadic Green's function has the explicit form

$$\tilde{\overset{\leftrightarrow}{G}}_o(\vec{r}',\vec{r}'';s) = \frac{\gamma}{4\pi} e^{-\zeta} \left\{ \left[-2\zeta^{-2} - 2\zeta^{-3} \right] \vec{1}_R \vec{1}_R \right.$$

$$\left. + \left[\zeta^{-3} + \zeta^{-2} + \zeta^{-1} \right] \left[\overset{\leftrightarrow}{1} - \vec{1}_R \vec{1}_R \right] \right\} + \frac{1}{3\gamma^2} \delta(\vec{r}' - \vec{r}'') \overset{\leftrightarrow}{1}$$

(3.10)

$\overset{\leftrightarrow}{1} \equiv$ identity dyad

$$\vec{1}_R \equiv \frac{\vec{r}' - \vec{r}''}{|\vec{r}' - \vec{r}''|} \qquad \text{for } \vec{r}' \neq \vec{r}''$$

where the delta function is introduced so that the remaining part can be handled in (3.8) as a principal value integral with a small spherical zone of exclusion centered on $\vec{r}' = \vec{r}''$ (ref. 3).

For our present purposes we assume that the distance from source to observer is large compared to the size of the source, i.e.,

$$\vec{r}' = \vec{0}$$

(3.11)

$$r'' \equiv |\vec{r}''| \simeq r \gg |\vec{r}' - \vec{r}''|$$

where $\vec{r}$ is taken as some effective center of the source. Furthermore we assume that frequencies of interest are sufficiently high that only the leading term for large r'' (the $|\vec{r}' - \vec{r}''|^{-1}$ or ζ^{-1} term in (3.10) need be included giving

$$\tilde{\overset{\leftrightarrow}{G}}_o(\vec{r}',\vec{r}'';s) \simeq \frac{e^{-\gamma |\vec{r}' - \vec{r}''|}}{4\pi |\vec{r}' - \vec{r}''|} \overset{\leftrightarrow}{1}_t$$

$$\simeq \frac{e^{\gamma \vec{1}_R \cdot r''}}{4\pi r} \overset{\leftrightarrow}{1}_t$$

(3.12)

$$\overleftrightarrow{1}_t \equiv \overleftrightarrow{1} - \vec{1}_R \vec{1}_R \equiv \text{transverse dyad}$$

Now referring to figure 3.1 we can approximate as

$$\vec{1}_R \simeq \vec{1}_1 = -\vec{1}_r$$

$$\overleftrightarrow{1}_t \simeq \overleftrightarrow{1} - \vec{1}_1 \vec{1}_1 = \overleftrightarrow{1} - \vec{1}_r \vec{1}_r \tag{3.13}$$

This allows us to write (from (3.8))

$$\tilde{\vec{E}}_{inc}(0,s) \simeq - \frac{\mu_o e^{-\gamma r}}{4\pi r} \overleftrightarrow{1}_t \cdot \tilde{\vec{T}}(s)$$

$$\tilde{\vec{T}}(s) \simeq s \int_V e^{\gamma(r - \vec{1}_r \cdot r'')} \tilde{\vec{J}}(\vec{r}'',s) \, dV'' \tag{3.14}$$

In time domain we have

$$\vec{T}(t) \simeq \frac{\partial}{\partial t} \int_V \vec{J}(\vec{r}'', t + \frac{1}{c}(r - \vec{1}_r \cdot \vec{r}'')) \, dV'' \tag{3.15}$$

This $\vec{T}$ can be thought of as a kind of effective source vector. Assuming that changes in $\vec{J}$ propagate over the source volume at velocities slow compared to c we have

$$\tilde{\vec{T}}(s) \simeq s \int_V \tilde{\vec{J}}(\vec{r}'', s) \, dV''$$

$$\vec{T}(t) \simeq \frac{\partial}{\partial t} \int_V \vec{J}(\vec{r}'', t) \, dV'' \tag{3.16}$$

The magnetic field incident at $\vec{r}' = \vec{0}$ can be found by expanding from (3.8), or by simply noting that the far field ($|\vec{r}' - \vec{r}''|^{-1}$ term) has a plane-wave relation between the electric and magnetic field as

$$\tilde{\vec{H}}_{inc}(0,s) \simeq \frac{1}{Z_o} \vec{1}_1 \times \tilde{\vec{E}}_{inc}(0,s)$$

$$\simeq - \frac{e^{-\gamma r}}{4\pi rc} \vec{1}_1 \times \tilde{\vec{T}}(s) \tag{3.17}$$

In time domain the fields are

$$\vec{E}_{inc}(0,t) \simeq - \frac{\mu_o}{4\pi r} \overleftrightarrow{1}_t \cdot \vec{T}(t - \frac{r}{c})$$

$$\tag{3.18}$$

$$\vec{H}_{inc}(0,t) \simeq -\frac{1}{4\pi rc}\vec{1}_1 \times \vec{T}(t - \frac{r}{c})$$

Near $\vec{r}' = \vec{0}$ the incident field is an approximate plane wave propagating in the $\vec{1}_1$ direction; it can be represented as

$$\vec{E}_{inc}(\vec{r}',t) \simeq E_h(t - \frac{\vec{1}_1 \cdot \vec{r}'}{c})\vec{1}_2 + E_e(t - \frac{\vec{1}_1 \cdot \vec{r}'}{c})\vec{1}_3$$

$$\vec{H}_{inc}(\vec{r}',t) = \frac{1}{Z_o}\left\{E_h(t - \frac{\vec{1}_1 \cdot \vec{r}'}{c})\vec{1}_3 - E_e(t - \frac{\vec{1}_1 \cdot \vec{r}'}{c})\vec{1}_2\right\}$$

(3.19)

This decomposes the fields incident at the observer into two parts, an E wave (or TM wave) denoted by a subscript e, and an H wave (or TE wave) denoted by a subscript h. This decomposition is based on the polarization with respect to the z axis (i.e., a TM wave has the magnetic field perpendicular to the z axis, and a TE wave has the electric field perpendicular to the z axis).

Now when the incident fields reach the ground plane (the x,y plane), the conducting ground plane reflects the fields so that (at least at the higher frequencies because of the finite dimension of the ground plane on the earth) approximately we have

$$E_z \simeq 2\vec{1}_z \cdot \vec{E}_{inc}$$

$$H_x \simeq 2\vec{1}_x \cdot \vec{H}_{inc} = H_N = -H_S$$

(3.20)

$$H_y \simeq 2\vec{1}_y \cdot \vec{H}_{inc} = H_W = -H_E$$

The remaining three fields components are approximately zero. Note the orientation of the cartesian coordinates with respect to the (geographical) compass positions (north $\equiv$ N, east $\equiv$ E, south $\equiv$ S, west $\equiv$ W).

On the ground plane we then have

$$E_z = 2\sin(\theta)E_e$$

$$H_\phi = -H_2 = \frac{2}{Z_o}E_e$$

(3.21)

$$H_\psi = -\cos(\theta)H_3 = -\frac{2}{Z_o}\cos(\theta)E_h$$

Then construct

$$\frac{1}{2}E_z = \sin(\theta)E_e$$

$$\frac{Z_o}{2} H_\phi = \frac{Z_o}{2} \{-H_x \sin(\phi) + H_y \cos(\phi)\} = E_e \qquad (3.22)$$

$$\frac{Z_o}{2} H_\psi = \frac{Z_o}{2} \{H_x \cos(\phi) + H_y \sin(\phi)\} = -\cos(\theta) E_h$$

From our measurements we have three pieces of information: E_z, H_x, and H_y. We have four unknowns: E_e, E_h, θ, and ϕ.

If we knew the source angles (θ, ϕ), or at least one of these, then the two waves E_e and E_h could be constructed. Let us for the moment assume that θ and ϕ are known. From (3.18) and (3.19) together with E_e and E_h we can find

$$\overleftrightarrow{1}_t \cdot \vec{T}(t - \frac{r}{c}) = -\frac{4\pi r}{\mu_o} \vec{E}_{inc}(0, t)$$

$$= -\frac{4\pi r}{\mu_o} \left\{ E_h(t) \vec{1}_2 + E_e(t) \vec{1}_3 \right\} \qquad (3.23)$$

This shows that we can obtain the relative strength of the transverse (2 and 3) components of the source $\vec{T}$ by comparing E_h and E_e. Referring to figure 3.1B one can plot on such a diagram an angle that $\vec{T}$ makes with respect to say $\vec{1}_3$ as another vector on the plane perpendicular to $\vec{1}_1$. Note that the 1 component of $\vec{T}$ is not obtained in this technique since it does not appear in the far-field expansion at $\vec{r}' = \vec{0}$. If one knew r then the 2 and 3 components of $\vec{T}$ would be completely known. Techniques for estimating r are discussed in another section of this paper. Having r then one can use (3.23) to find T_2 and T_3; this is used for later plots of the transverse part of $\vec{T}$.

Having $\overleftrightarrow{1}_t \cdot \vec{T}$ one can also make some estimates concerning currents in the fast pulses in the source region near $\vec{r}$ by writing

$$\vec{T} \equiv \overrightarrow{(I \, v_{eff})} = \Delta \left\{ \frac{\partial}{\partial t} \int_{V''} \vec{J}(\vec{r}'', t) \, dV'' \right\} \qquad (3.24)$$

Here Δ indicates the change in the quantity; for later plots this is the change from the ambient value before a fast pulse to the peak of the pulse. (This convention is employed for $\partial \vec{T}/\partial t$ also.) An effective streamer speed v_{eff} can be used to obtain some indication of the current I, or at least some rough bound on it.

Now consider the determination of θ, ϕ. Figure 3.2 shows a type of display of coordinates which is useful for our purposes. Superimposed on the cartesian directions and compass coordinates we have a polar plot in which θ is the radial coordinate with $0^0 \le \theta \le 90^0$. The azimuthal coordinate is ϕ with $0 \le \phi < 360^0$.

Returning to (3.22) our three measurements (E_z, H_x, H_y) can be used to find a relationship between θ and ϕ. Specifically the first two of (3.22) can be used to eliminate E_e giving

$$Z_o \left\{ -H_x \sin(\phi) + H_y \cos(\phi) \right\} = \frac{E_z}{\sin(\theta)} \tag{3.25}$$

as our θ,ϕ relation. Constraining $0 \le \theta \le 90^0$ and ϕ real gives a curve in the θ,ϕ "plane" of acceptable solutions of (3.25). For each pulse we can consider the change in the fields (ambient to peak) in (3.25) or some other aspect of the pulse waveforms. Besides the field change we have used the change in the time derivatives of the fields ($\partial E_z/\partial t$, $\partial H_x/\partial t$, $\partial H_z/\partial t$) in (3.25) to determine the θ,ϕ curves. Both the field changes and changes in field time derivatives (on the rise of the pulses) typically give comparable results, as will be seen later.

A special case is encountered if the incident field is a pure H wave (i.e., $\vec{E}$ parallel to the ground plane). In this case $E_e = 0$. From (3.22) we have

$$\tan(\phi) = \frac{H_y}{H_x} \tag{3.26}$$

which has two solutions for ϕ separated by 180^0. In the θ,ϕ "plane" in figure 3.2 this gives a locus of solutions a "straight line" passing through the zenith ($\theta = 0$).

Having a contour in the θ,ϕ "plane" resulting from a particular measured fast electromagnetic-field pulse (or its time derivative) one would like to find some point along that contour that represents the true angles θ,ϕ to the source. One way to do this uses an assumption that another pulse in a particular recording (about 20 μs wide in the presented data) comes from approximately the same source location. This is physically reasonable if one considers a leader propagating through the air to establish the lightning channel. If each pulse represents some brief extension of the arc channel, and if the distance the streamer propagates during the pulse is small compared to the distance to the observer, then the change in (θ,ϕ) is small. Furthermore, if the two pulses under consideration have different polarizations (different proportions of E and H waves) due to different directions of $\vec{1}_t \cdot \overset{\leftrightarrow}{T}$, then (3.25) will give in general different θ,ϕ contours for the two pulses. The intersection of the two contours can then be taken as an experimental determination of (θ,ϕ) for both pulses.

Going further, it will be observed in considering the data that the intersection of θ,ϕ contours is remarkably successful in determining (θ,ϕ) values. In some cases all the θ,ϕ contours (of the order of ten contours) can all pass quite near a common (θ,ϕ) approximate intersection. In other cases subsets of the contours for a particular waveform set form a few distinct approximate (ϕ,θ) values. Some cases are presented in the data illustrating some of the complexity that can be unravelled in this way.

Having determined the (θ,ϕ) values appropriate to particular pulses, and estimating the corresponding r, one goes back to (3.22) to find E_e and E_h (or their derivatives with respect to time). Then (3.23) gives the transverse components of $\overset{\leftrightarrow}{T}$ for plots with respect to the $\vec{1}_2$ and $\vec{1}_3$ directions as in figure 3.1B.

IV.   ESTIMATION OF RANGE TO LIGHTNING CURRENT PULSES

The electric field changes produced by lightning in this study were also sensed with a "slow antenna" field change meter and recorded onto FM magnetic tape, together with the IRIG B, 1 kHz time code that was distributed to coordinate the thunderstorm and lightning measurements. This time code was synchronized with Radio Station WWV and permitted the slow measurements to be correlated with a time resolution of 1 ms. A Globe 100 B microphone with an extended low frequency response was mounted on the metal mesh adjacent to the Kiva and was used to detect the arrival of thunder. The thunder signals were recorded on a second FM magnetic tape channel. In this manner, the time of occurrence, the nature of the lightning flash and the time from flash-to-thunder could be determined.

Two acoustic arrays, each consisting of three microphones at the vertices of 30 m, equilateral triangles were located in the meadow, south of the Kiva. (See Figure 1.1.) The time-difference of arrival of individual thunder peals across each of these triangular arrays permitted a determination of the direction cosines for the normal to the acoustic wave front. With these and the distance from each source to the array calculated from the speed of sound and the time interval from field change to peal arrival, a first estimate could be made for location of each source. Corrections were then made for the local winds and for thermal refraction in a second approximation for the source location using the technique described by Winn et al. (ref. 4).

In addition to the use of these acoustic techniques for the location of lightning, the flashes in the vicinity of the Kiva were video-recorded with a time resolution of 16 ms per TV frame. One TV camera recorded the view from an all-sky reflecting, parabolic mirror located on top of South Baldy peak about 50 m north of the Kiva, while another TV system located at Langmuir Laboratory recorded the view of lightning over South Baldy peak as seen from 2 km to the SSE.

These video recordings have been played back, frame by frame, onto a video monitor where they were photographed together with an output displaying the IRIG B time code that was also recorded on the audio tracks of the video tape recorders.

All of the flashes reported in this study were "cloud-to-ground" discharges. Our first approximation for the slant range from the Kiva to the lightning current element of interest is based on the assumption that the time from flash to thunder multiplied by the speed of sound in air gives the horizontal distance from the Kiva microphone to the closest part of the lightning channel (that is striking the earth approximately vertically).

From section 3, the zenith angle θ and the azimuth angle ϕ can be estimated for the current element from the electromagnetic signal that it produced.

The approximate slant range r from the Kiva to the current element is therefore given by

$$r \simeq (336 \text{ m/s})(\Delta t)/\sin(\theta) \tag{4.1}$$

The cartesian coordinates of the current element are therefore

$$x = (336 \text{ m/s})(\Delta t) \cos(\phi), \quad \text{toward the north}$$

$$y = (336 \text{ m/s})(\Delta t) \sin(\phi), \quad \text{toward the west} \tag{4.2}$$

$$z = r/\cos(\theta), \quad \text{above the Kiva}$$

In the four cases to date in which we have compared the thunder source maps with current element coordinates, there has been a fair agreement between the two somewhat independent location systems. If the range chosen from the horizontal distance assumption is too small, a better estimate for the range can be extracted from the intersection of the vector $\vec{r}$--directed along the calculated values of θ and ϕ--with the thunder channels mapped by the acoustic technique.

V. ANALYZED WAVEFORMS

In this section the techniques discussed in sections 4 and 5 are applied to some example data sets for four selected waveforms.

A. Rocket-Triggered Lightning

Our first example is given in figures 5.1 through 5.8. It is a good example of leader-like behavior and is associated with a triggered lightning event. The lightning stroke was triggered by a wire-trailing rocket launched from the position indicated in figure 1.1 which is 350 m in horizontal range at an azimuth of $\phi = 155^0$ with respect to the Kiva. The rocket was launched approximately vertically. Based on visual observations its height was estimated as about 600 m above the Kiva when it initiated a lightning discharge. This corresponds to a zenith angle of $\theta \simeq 30^0$ with respect to the Kiva. Based on the extreme electric-field enhancement at the rocket, it was expected that the streamer direction of interest was upward, beginning from the rocket. This polarity is assumed later in the data analysis.

Looking at figure 5.1 we see the leader-like behavior on the 20 µs waveform for the three derivative field components. For convenience 9 pulses are identified by numbers corresponding to their peak times of occurrence (within the record event) in microseconds; the north component of $\partial \vec{B}/\partial t$ had the generally largest pulses and was used for this labelling. Figure 5.2 results from the numerical integration of the digital data from which figure 5.1 was produced. Here the pulses are also identified (on the east component of $\vec{B}$ in this case). Note the general drift in the baseline which may be partially due to a little offset in the recording of the derivative data, but probably is a result of a continuing current flowing up the channel initiated by the rocket.

Figure 5.3 shows the slow changes in the electric field, first from the rising of the grounded wire, followed by the emission of upward-going positive streamers. Also shown is a recording of the narrowband RF power received centered on 34 MHz, as measured by a different experiment (Hayenga) with a complex antenna pattern. For our purposes it is interesting to note that the RF power emissions began at about 0.6 s after rocket launch indicating some corona-like discharges before the main lightning event.

The acoustically determined (per section 4) thunder sources are displayed in figure 5.4. This indicates that the lightning discharge turned south and extended about 4 km at a height of about 2 km. This can be compared to the whole-sky video-tape photograph in figure 5.5B obtained at the balloon hanger (fig. 1.1) about 700 m south of the rocket launcher. This indicates the main streamer rising and propagating to the south near cloud-base level at a height of about 1 km. Figure 5.6B shows the same event at about 160 ms later. Note in the whole-sky photographs the TV camera in the center since it is above a paraboloidal mirror.

The θ,ϕ contours from the nine pulses identified for the derivative waveform in figure 5.1 are displayed in figure 5.5A. This shows a remarkably tight set of intersections in which all 9 contours pass through nearly the same point. The estimated angles from the Kiva to the source are $(\theta,\phi) \simeq (30^0, 177^0)$. This is in quite good agreement with the estimated rocket position. The major difference is in azimuth (177^0 vs 155^0), but there are uncertainties in the exact position of the rocket because it impacted to the south near the comet observatory (fig. 1.1), despite its near vertical aiming. The slant range is estimated as $r \simeq 700$ m based on $\theta = 30^0$ and a horizontal distance of 350 m. The same contours, except now based on the field (numerically integrated) waveform are shown in figure 5.6A. Here the intersection is not so tightly clustered indicating that more accuracy is generally obtained from the derivative-format data. This is not surprising since the analysis is based on a high-frequency approximation and because the integration has some error. For comparison the estimated source location (based on the derivative data) is superimposed on the plot of acoustic source locations in figure 5.4.

Now we reconstruct the source. In figure 5.7 the derivative waveform with the estimated $\vec{r}$ (as discussed) is used to find the peak values of the $\partial\vec{T}/\partial t$ pulses. Figure 5.7B shows the individual vector pulses (as seen from the Kiva) oriented to the right and slightly downward. Assuming that the streamer velocity $\vec{v}_{eff}$ is parallel to $\vec{J}$ and in the same direction for this case we have the effective reconstruction of the positive streamer in figure 5.7A. For this type of assumed positive streamer, denoted by $\vec{v}_{eff} \uparrow\uparrow \vec{J}$ we take the individual vector pulses in their order of occurrence and lay them out from the graph origin sequentially in a cumulative manner (tail of vector coincident with head of previous vector). Figure 5.8 does the same thing for the $\vec{T}$ pulses from the field waveforms and gives a comparable picture.

While this lightning event was a positive-going streamer, it is interesting to note that the impulsive nature of the fields is similar to that of natural negative step leaders.

B. Midrange Leader(s)

Our second example is given in figures 5.9 through 5.21. As will be seen this is a case of significant branching. For sake of a label let us refer to this case as "midrange leader(s)." Figures 5.9 and 5.10 show the derivative fields and fields for the 20 μs record indicating leader-like behavior.

Figure 5.11 shows the slow electric field and thunder microphone records from which a horizontal range of 400 m is estimated. Figure 5.12 gives the acoustic source reconstruction indicating an interesting streamer-path structure. Extending from about 3 km height, about 3 km to the east (slightly north of east), the pattern divides at about 2.5 km above the Kiva and descends to the mountain in at least three major channels. On this is superimposed three EM source locations determined from the derivative waveform.

The whole-sky video-tape photographs in figures 5.13B and 5.14B show these three channels quite clearly as seen from the Kiva. Figure 5.14B corresponds to 32 ms later than figure 5.13b.

Looking at the θ, ϕ contours in figure 5.13A from the derivative waveform in figure 5.9, we do not see all the contours passing near a common (θ, ϕ). It appears that several sources are located above the Kiva. From figure 5.13A three (θ, ϕ) values were found as indicated on the figure. These angles are combined with the horizontal range of 400 m to give the estimated EM source locations in figure 5.12. As an aid in identifying the three sets of pulses corresponding to the three locations, the directions of $\partial\vec{T}/\partial t$ were considered so as to have all the $\partial\vec{T}/\partial t$ pulses in a particular set have the same general direction (as in figures 5.15 through 5.17).

Considering the field waveform in figure 5.10 the plot of θ, ϕ contours in figure 5.14A was made. Here four sets of pulses were identified. Sets 1, 2, and 3 correspond reasonably to those from the derivative waveforms as do the directions of the $\vec{T}$ pulses as compared to the corresponding $\partial\vec{T}/\partial t$ pulses. Set 4 in figure 5.14A was defined based on a disagreement in the direction of $\vec{T}$ pulses from those in set 1 as based on the directions in figures 5.18 and 5.21. However, noting the small θ values for this case the change in ϕ still corresponds to only a small distance change on the unit sphere, but a large rotation of the unit vectors $\vec{1}_2, \vec{1}_3$. Identifying these set 4 $\vec{T}$ pulses with the corresponding $\partial\vec{T}/\partial t$ pulses it appears that set 4 pulses likely belong combined with set 1.

Since set 1 corresponds to small θ an estimate of slant range based on 400 m horizontal range is likely in error because the lightning arc is not exactly vertical. Based on figure 5.12 the lower heights as in figure 5.15 for $\theta = 20^0$ are more reasonable. This is consistent with relying more on $\partial\vec{T}/\partial t$ data for θ, ϕ determination.

For this negative step leader we have $\vec{v}_{eff} \uparrow\downarrow \vec{J}$ (antiparallel). So in the effective streamer reconstruction in figures 5.15 through 5.21 the vectors for the sequential pulses are started from the graph origin with each vector head placed at the previous vector tail.

Note that values of $\vec{T}$ pulses depend on choice of r. For sets 1 and 4 r is clearly overestimated indicating the true T values are somewhat less (by perhaps a factor of 2) than indicated in figures 5.18 and 5.21.

C. Nearby Leader

Our third example is given in figures 5.22 through 5.31. This is labelled "nearby leader." Figures 5.22 and 5.23 show the derivative fields and fields for the 20 µs record.

Figure 5.24 shows the slow electric field and thunder microphone records, from which a horizontal range of 95 m is estimated. Figure 5.25 gives the acoustic source reconstruction indicating one principal streamer channel near the Kiva. Extending from about 5 km height there is some branching also collecting charge about 1.5 km a little north of west. On this is superimposed the location of the two EM sources which were very close together on this scale. Figures 5.26B and 5.27B show the same whole-sky video-tape photograph indicating a channel to the west. Noting that this whole-sky camera is not exactly at the Kiva, but about 50 m north of it on the highest point of South Baldy peak (see fig. 1.1) the several channel location techniques give quite good agreement.

Looking at the θ, ϕ contours for derivative data in figure 5.26A we find two approximate sets of contour intersections. This was aided by noting the direction of $\partial \vec{T}/\partial t$ pulses in figures 5.28 and 5.29. Figure 5.27A does the same for the field waveform pulses with good agreement, including the directions of the $\vec{T}$ pulses in figures 5.30 and 5.31.

Noting the two sources approximately above and below each other, these appear to be on or near the same main channel. It is conceivable that the lower source is a positive streamer and the upper streamer a negative one with the two streamers heading toward each other. For the plots of the $\partial \vec{T}/\partial t$ and $\vec{T}$ pulses in figures 5.28 through 5.31 we have chosen the convention $\vec{v}_{eff} \uparrow\downarrow \vec{J}$ since such an above possibility is difficult to confirm.

D. Return Stroke

Our fourth example is given in figures 5.32 through 5.39. This is labelled "return stroke" based on the wide (1 µs) pulses as indicated in figure 5.33, as well as the sustained deviation of the later-time portions of the waveform. Figures 5.32 and 5.33 show the derivative fields and fields for the 20 µs records.

Figure 5.34 shows the slow electric field and thunder microphone records, from which a horizontal range of 1775 m is estimated. Figure 5.35 gives the acoustic source reconstruction indicating two possible closures to ground. Extending from about 4 km height a little north of east of the Kiva the channel approaches the Kiva striking the ground about 2 km due east. On this is superimposed the estimated locations of the EM source, one each for the derivative waveform and the field waveform. Figures 5.36 and 5.37 show the same whole-sky

video-tape photograph indicating a channel to the east, in agreement with the acoustic source location.

Looking at the θ, ϕ contours for derivative data in figure 5.36A we find a single approximate contour intersection somewhat north of east and at a high elevation. Similar results are found from the field waveform pulses in figure 5.37A. These two (θ, ϕ) values are combined with the horizontal range to give the two estimates for the source location in figure 5.35. Note, however, that the lightning channel is not vertical and the true source location is likely to be farther to the east, and at a high elevation, unless some branching occurs back toward the west.

Figures 5.38 and 5.39 give the rough streamer reconstruction based on $\partial \vec{T}/\partial t$ and $\vec{T}$ respectively. The streamer is assumed positive, i.e., $\vec{v}_{eff} \uparrow\uparrow \vec{J}$, in keeping with the character of a return stroke. Note, however, the high elevation. This return-stroke corresponds to a large and wide current pulse in the clouds. A larger range (as is possible) would give larger $\partial \vec{T}/\partial t$ and $\vec{T}$ pulses than indicated in figures 5.38 and 5.39.

E. Some Comments

These four examples give representative characteristics of lightning near South Baldy peak. Many more recordings were obtained. It is anticipated that a significant fraction of these will be analyzed for future publication. These include both leader-like examples and return-stroke-like examples, including events near the horizon which appear to be more classical return strokes.

From the examples given the values of $\vec{T}$ have magnitudes (from transverse components) of about 2×10^{12} Am/s for return strokes to about 5×10^{11} Am/s for leader-like sources (noting order of magnitudes and directions of streamers toward (or away from) the observer at the Kiva). Assuming a v_{eff} of about 10^8 m/s gives 20 kA for return strokes and 5 kA for leader-like pulses. These are very variable and the number is quite approximate. Further analysis of the data may shed more insight into such results.

For these data all the lightning events represent negative charge being, in effect, lowered to earth. It would be interesting to see what would occur in the rare event of positive charge being lowered to earth.

In the recordings for the three components of field time derivative at the Kiva the peaks did not occur at exactly the same time. The separation of the sensors on the ground plane was about 11 ns, and the difference in cable transit times was about 14 ns, giving a maximum time shift of about 25 ns. This resulted in peaks on the digital printout having a relative time displacement of up to three time intervals, or 30 ns, as was observed. For the present analysis the actual peaks of the individual components, regardless of time, were used.

Unfortunately the trigger signal for the Biomation recorders was not recorded on magnetic tape in 1979, whereas it had been so recorded in 1978. This would have given even more definitiveness to the interpretations of the

3-component 1979 data. However, analysis of 1978 waveforms does indicate that to the 1 ms tape resolution, the waveforms all correspond to the first return stroke or the leader-like anticipation of this return stroke.

VI. SUMMARY

As the foregoing data and associated data analysis has indicated, fast nuclear-EMP related sensors and appropriate fast transient recorders have much to offer for the measurement and associated understanding of lightning electromagnetic environments. The lightning and nuclear EMP phenomena have some similar characteristics because of their common nature as transient electromagnetic phenomena.

In this report we have discussed some of the results obtained concerning lightning environments from our measurements using such instrumentation on South Baldy peak. Three electromagnetic field components (one electric, two magnetic) were measured on a ground plane with 10 ns resolution for recording times of about 20 μs. By comparing the three field components to each other, and by the use of acoustic ranging, the lightning electromagnetic sources were approximately located and their characteristics were studied.

The individual lightning waveforms yielded information concerning the temporal characteristics of leader electromagnetic fields. Pulse widths of the electromagnetic field individual pulses varied from about half a microsecond to less than 100 ns. Characteristic times for the rise (peak field divided by peak derivative) varied from something approaching 100 ns to something less than 30 ns; rise times were a little longer than these characteristic times for the rise.

Information was also obtained concerning the temporal characteristics of return-stroke electromagnetic fields. Pulse widths (of the magnetic field) of the order of 1 μs were observed, and rise times less than 100 ns were also observed. Characteristic times for the rise of the order of 50 ns were observed.

Comparing the fast electromagnetic-field pulses from leaders and return strokes at comparable distances from source to observer shows that the return-stroke field waveforms have generally larger amplitudes than those for leaders. However, for the time derivatives of the electromagnetic fields, the amplitudes for leaders and return strokes are quite comparable.

Combining the three electromagnetic-field time-derivative waveforms (or their time integrals) one can obtain for each pulse a relation between θ and ϕ giving a contour in the θ,ϕ "plane." Intersections of such contours can give approximate (θ,ϕ) values for source location providing the corresponding pulses originate from nearly the same locations. With location, source orientation (current density transverse polarization) can then be determined. Acoustic data can be used to estimate distances to these sources. The source vectors $\overset{\leftrightarrow}{1}_t \cdot \overset{\leftrightarrow}{T}$ (their peaks or peak time derivatives) can then be plotted to see how the current

direction changes from pulse to pulse. Connecting these vectors end to end gives a crude picture of the tortuousity of the leader path. From the magnitudes of the components of $\vec{T}$ one can obtain some information concerning currents and streamer speeds by giving these components the form Iv_{eff}. Typical current values of less than to greater than 10 kA are consistent with streamer speeds of the order of 10^8 m/s for leader strokes and return strokes respectively.

This data has some implications concerning the formulation of criterion lightning electromagnetic environment(s). The pulses encountered are significantly faster than a microsecond in their rise characteristics, even less than 100 ns. In terms of frequency spectrum this means much more high frequency content for the individual pulses. A detailed frequency spectral analysis of these kinds of pulses would be quite useful for the formulation of lightning electromagnetic criteria. One should note that these waveforms are not strictly applicable for direct-strike lightning since measurements were not made in such an environment. One may expect some of the presently observed environmental characteristics to apply in the direct-strike case, but this is not a full description.

The measurements reported here were made on South Baldy peak. Measurements at other geographical locations with different atmospheric conditions might reveal some differences in the electromagnetic waveforms from those obtained here. In the context of South Baldy peak more analysis of the existing data may reveal additional interesting features; additional waveforms are planned to be included in a future report. Future measurements may also obtain more complete lightning waveform information by finer time resolution, longer recording time windows, and/or additional and/or more accurate tie-ins with other physical phenomena.

REFERENCES

1.   Baum, C. E.: Emerging Technology for Transient and Broad-Band Analysis and Synthesis of Antennas and Scatterers. Interaction Note 300, November 1976, and Proc. IEEE, November 1976, pp. 1598-1616.

2.   Longmire, C. L.: On the Electromagnetic Pulse Produced by Nuclear Explosions. IEEE Trans. Antennas and Propagation, January 1978, pp. 3-13, and IEEE Trans. Electromagnetic Compatibility, February 1978, pp. 3-13.

3.   VanBladel, J.: Some Remarks on Green's Dyadic for Infinite Space. IRE Trans. Antennas and Propagation, November 1961, pp. 563-566.

4.   Winn, W. P., C. B. Moore, C. R. Holmes, and L. G. Byerley III,: Thunderstorm on July 16, 1975, Over Langmuir Laboratory: A Case Study. J. Geophysical Research, vol. 83, no. C6, June 20, 1978, pp. 3079-3092.

5.   Baum, C. E., E. L. Breen, C. B. Moore, J. P. O'Neill, and G. D. Sower: Electromagnetic Sensors for General Lightning Application. Symposium on Lightning Technology, NASA, Hampton, Virginia, U.S.A., 22-24 April 1980.
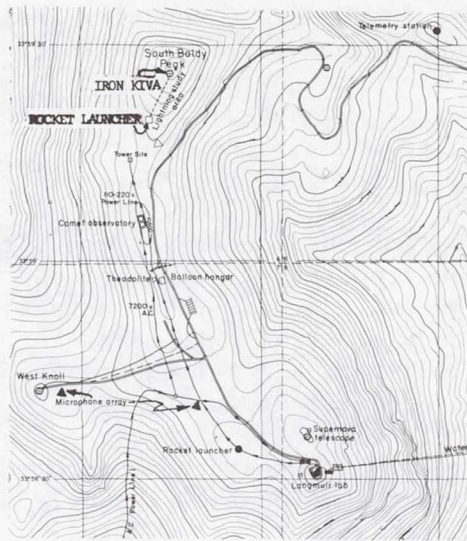
Iron Kiva altitude: 3275m. m.s.l.
map contour decrements: 13m

Figure 1.1.- Top view of electromagnetic and related measurement layout around South Baldy Peak, New Mexico.

east component of $\partial \vec{B}/\partial t$

east component of $\vec{B}$

Date: 79219 M.S.T.: 1022:51
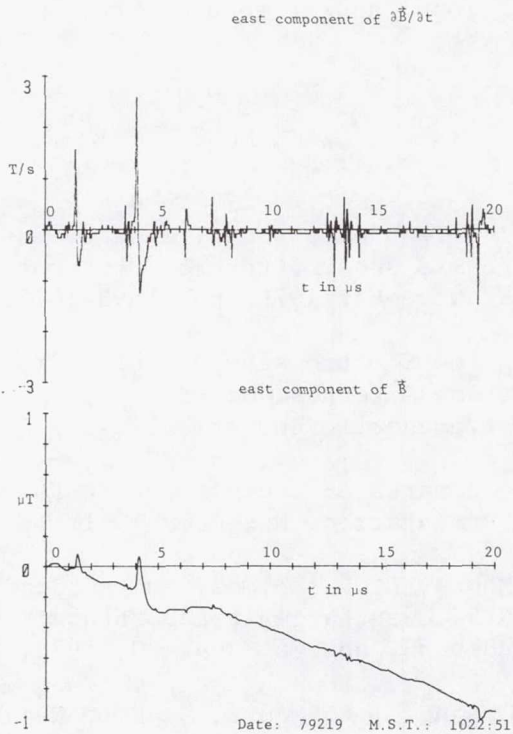
Figure 2.1.- Leader example: 20 µs scale.
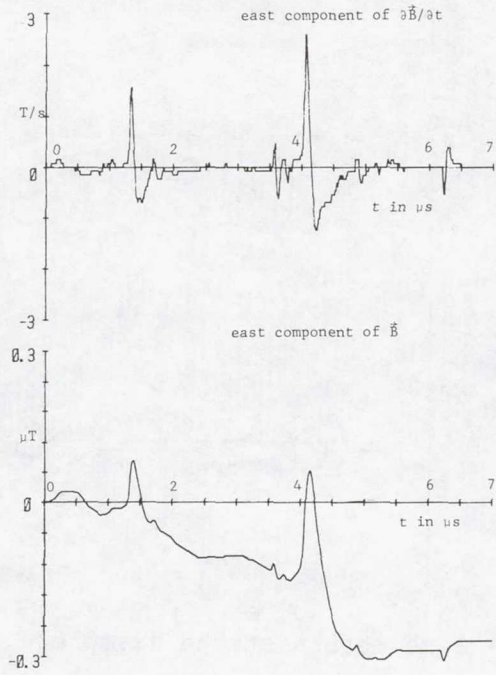
Figure 2.2.- Same leader example: 7 µs scale.

Date: 79219   M.S.T.: 1034:22
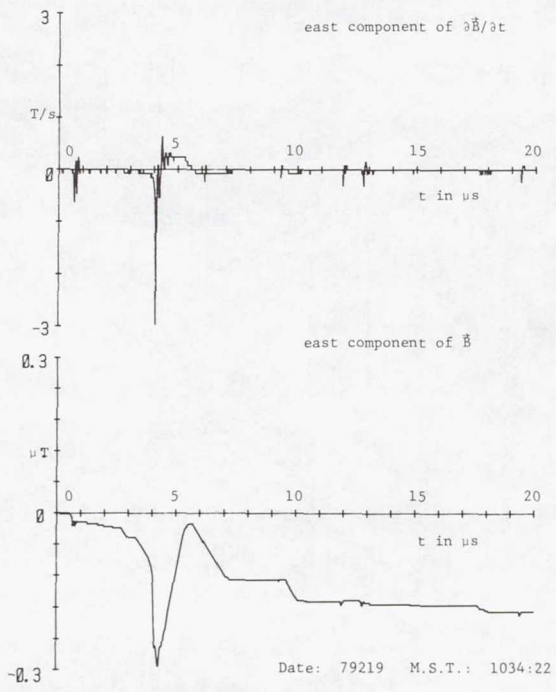
Figure 2.3.- Return-stroke example: 20 µs scale.

61

east component of $\partial \vec{B}/\partial t$
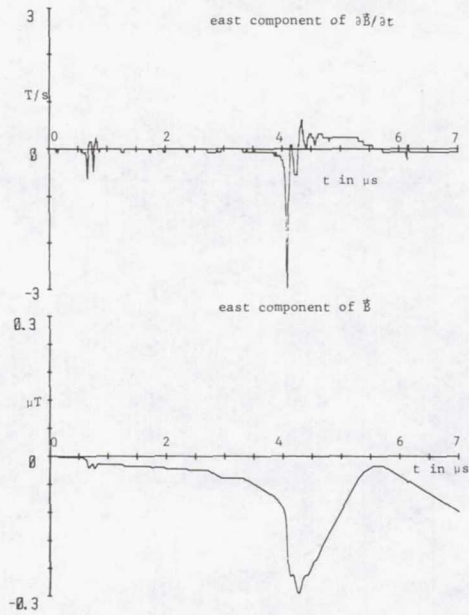
Figure 2.4.- Same return-stroke example: 7 μs scale.
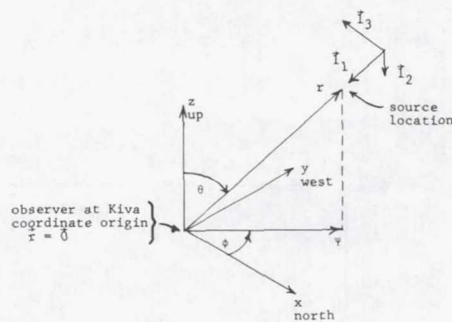
A. Coordinate systems
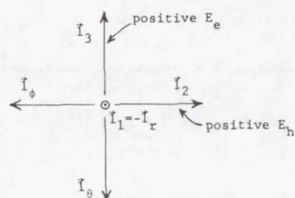
Figure 3.1.- Coordinates for lightning data analysis.
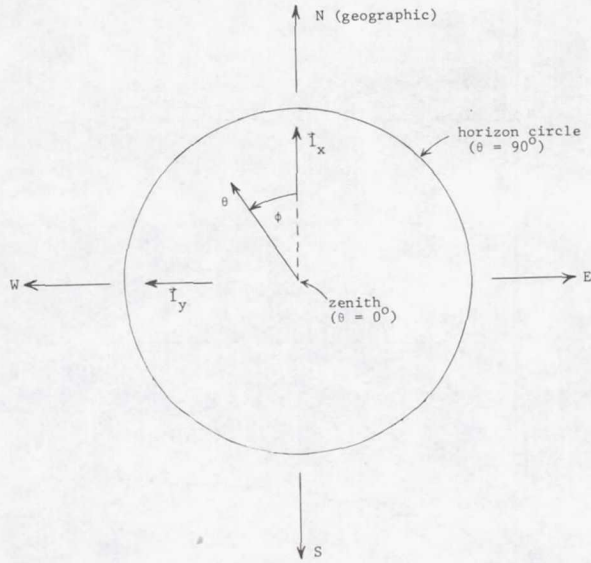
Figure 3.2.- Polar plot for determining direction to source.
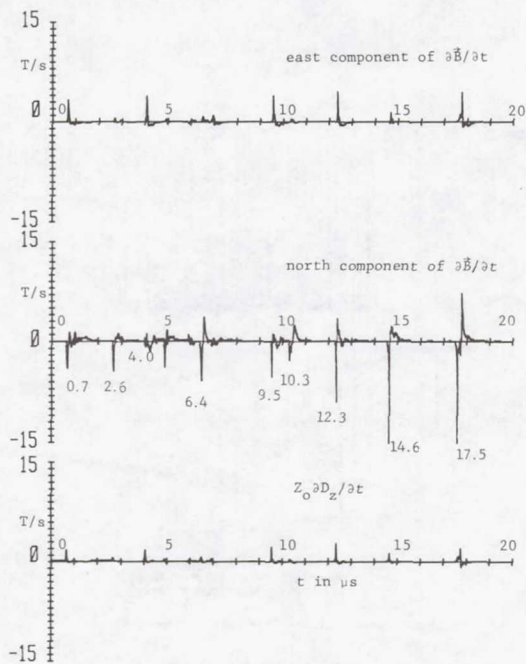
Date: 79228   M.S.T.: 1545:12

Figure 5.1.- Derivative fields from rocket-triggered lightning.
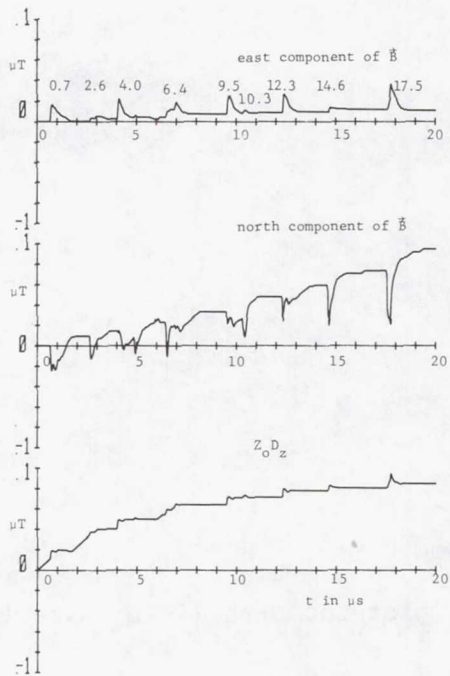
Date: 79228   M.S.T.: 1545:12

Figure 5.2.- Fields from rocket-triggered lightning.

Presumed time of trigger by
upward-going, positive streamer,
1.9 seconds after rocket launch

Horizontal range from Kiva to rocket launcher : 350 m
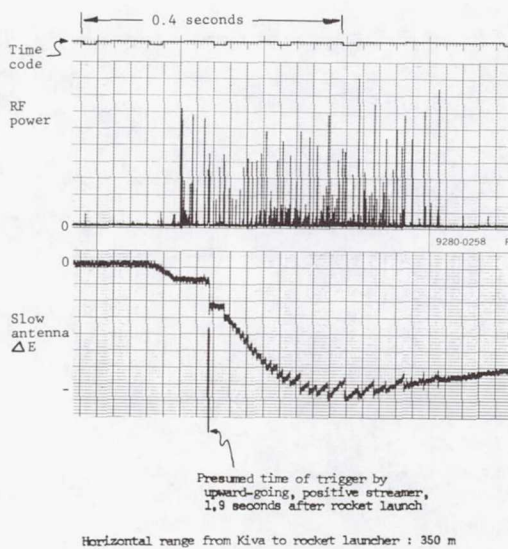
Date: 79228   M.S.T.: 1345:12

Figure 5.3.- Slow electric field change
and RF power received at 34 MHz from
rocket-triggered lightning.

ZENITH

ESTIMATED POSITION
OF EM SOURCE

NORTH

IRON KIVA

EAST

WEST

ROCKET LAUNCH POINT

LANGMUIR LAB

ticks on axes at 1 km intervals.

Date: 79228   M.S.T.: 1545:12

SOUTH
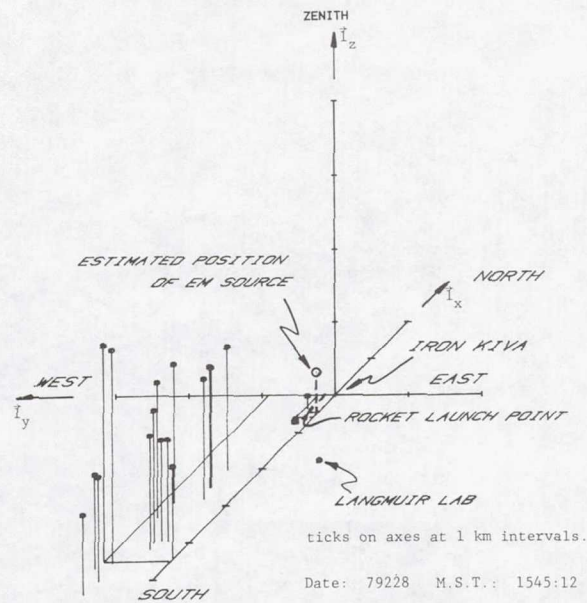
Figure 5.4.- Acoustic location of rocket-triggered lightning.

from derivative waveform

φ = 177°
θ = 30°

A. θ,φ contour plot

B. Whole-sky photograph from hangar   Date: 79228   M.S.T. 1545.12
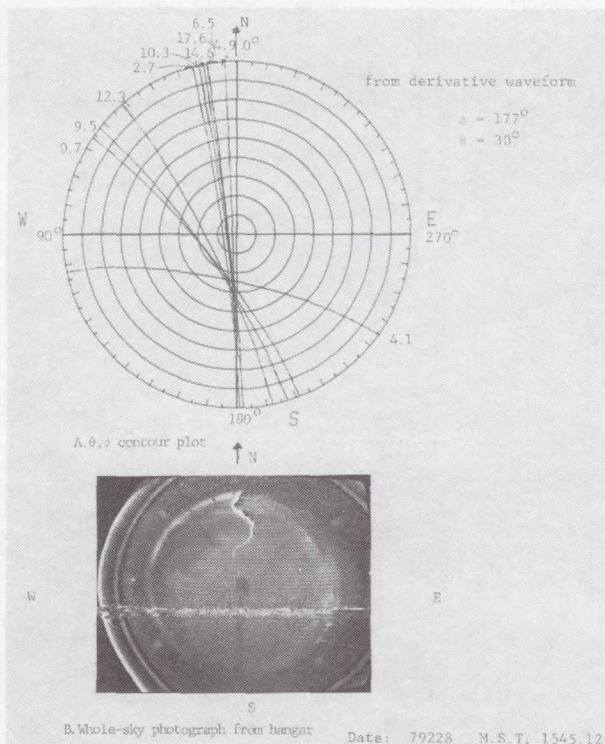
Figure 5.5.- θ,φ contours for rocket-triggered derivative waveform
and whole-sky videotape photograph.

A. θ,φ contour plot

N↑

W   E

S   Date: 79228 M.S.T.: 1545.12

B. Whole-sky photograph from hangar
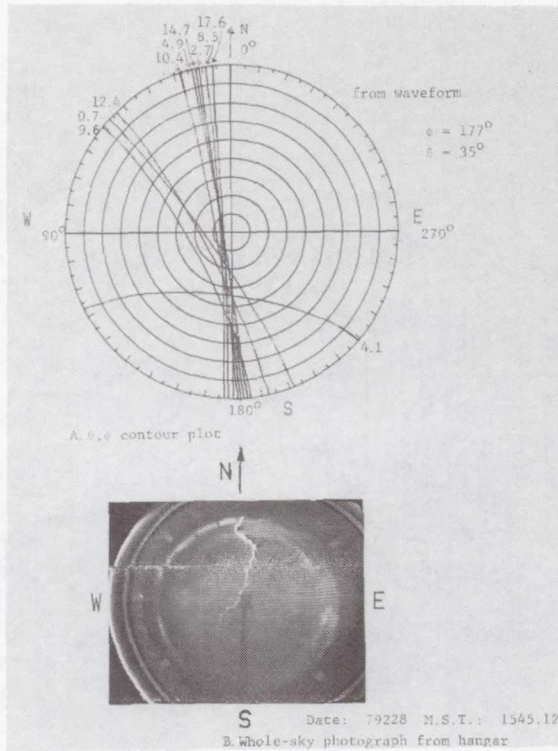
Figure 5.6.- θ,φ contours for rocket-triggered waveform and whole-sky videotape photograph.

A. Effective reconstruction of positive streamer

B. Peaks of $\partial \vec{T}/\partial t$

φ = 177°, θ = 30°, r = 700m

Date : 79228   M. S. T.: 1545: 12
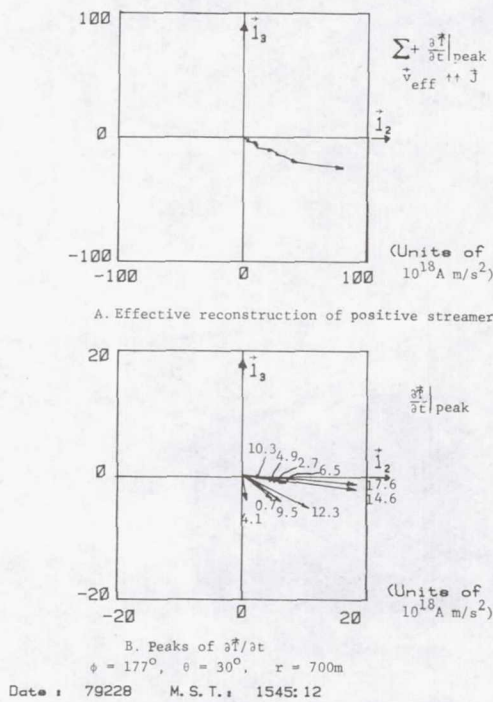
Figure 5.7.- $\partial \vec{T}/\partial t$ for rocket-triggered lightning.
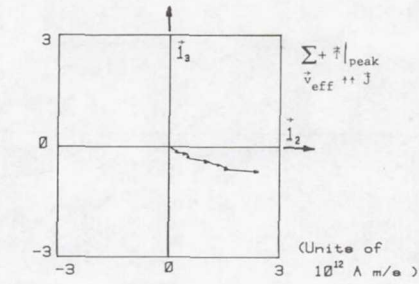
A. Effective reconstruction of positive streamer
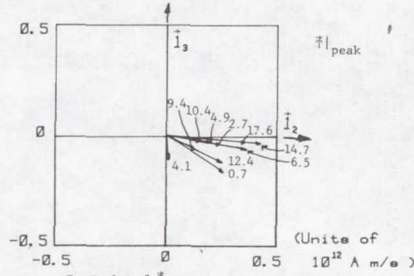
B. Peaks of $\vec{T}$

$\phi = 177°$, $\theta = 35°$, $r = 610$m

Date : 79228   M.S.T.: 1545:12

Figure 5.8.- $\vec{T}$ for rocket-triggered lightning.

east component of $\partial\vec{B}/\partial t$

north component of $\partial\vec{B}/\partial t$

Z_o $\partial D_z/\partial t$

t in μs
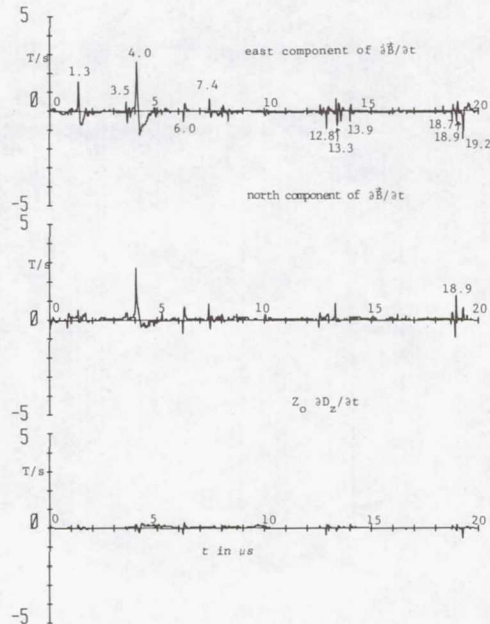
Date: 79219 M.S.T.: 1022:51

Figure 5.9.- Derivative fields from midrange leader(s).

Date: 79219   M.S.T.: 1022:51
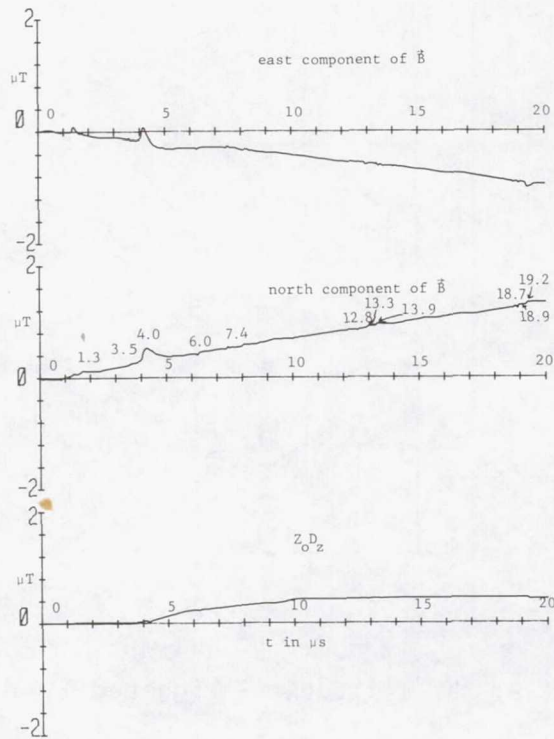
Figure 5.10.- Fields from midrange leader(s).

1.2 sec.
horizontal range = 400 m

Date: 79219   M.S.T.: 1022:51
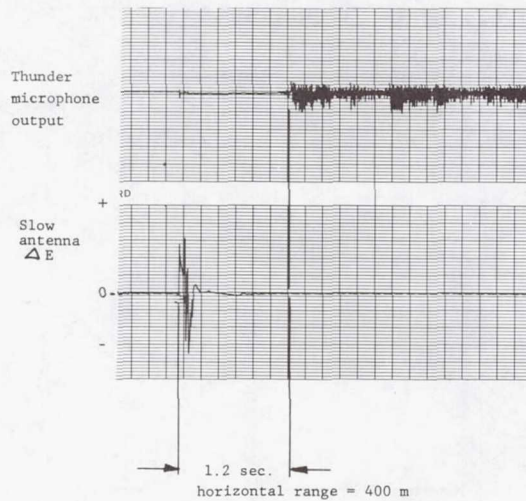
Figure 5.11.- Slow E field change and thunder microphone record
of midrange leader.

ZENITH

$\vec{1}_z$

ESTIMATED
POSITIONS
OF EM SOURCES

NORTH

$\vec{1}_x$

$\vec{1}_y$ WEST

1

2

EAST

LANGMUIR LAB

SOUTH

ORIGIN AT IRON KIVA
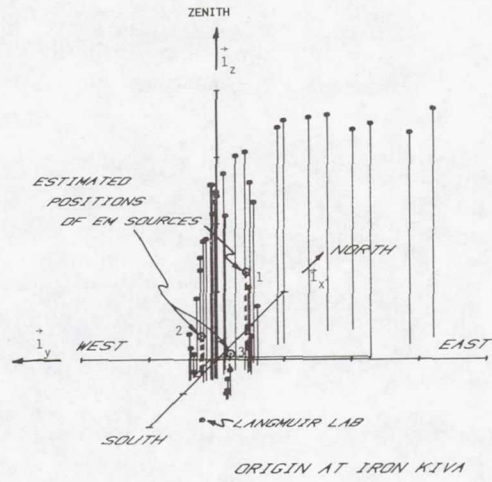
ticks on axes at 1 km intervals.

Date : 79219   M.S.T. : 1022:51

Note: Three lightning channels to earth
1,2,3 indicate set numbers of $\partial \vec{T}/\partial t$ pulses.

Figure 5.12.- Acoustic location of midrange leader(s).

A. θ, ϕ contour plot

B. Whole-sky photograph from Kiva
Date: 79219   M.S.T.: 1022.51
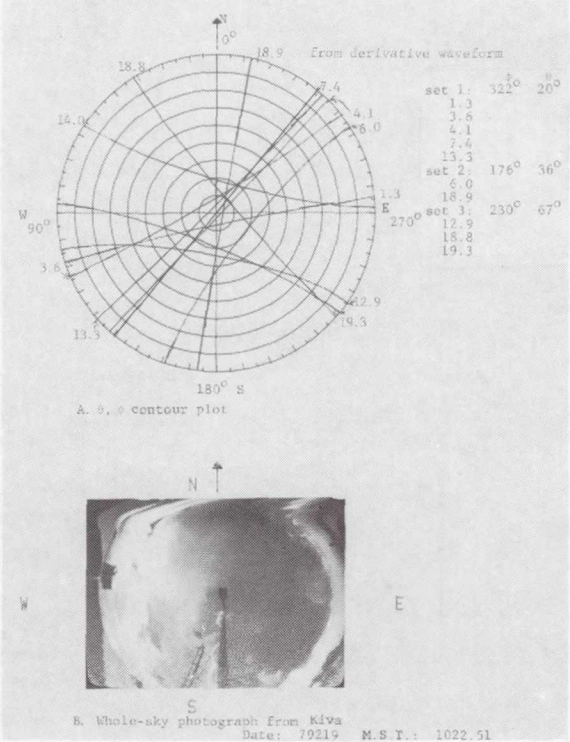
Figure 5.13.- θ,ϕ contours for midrange leader derivative waveform and whole-sky videotape photograph.

69
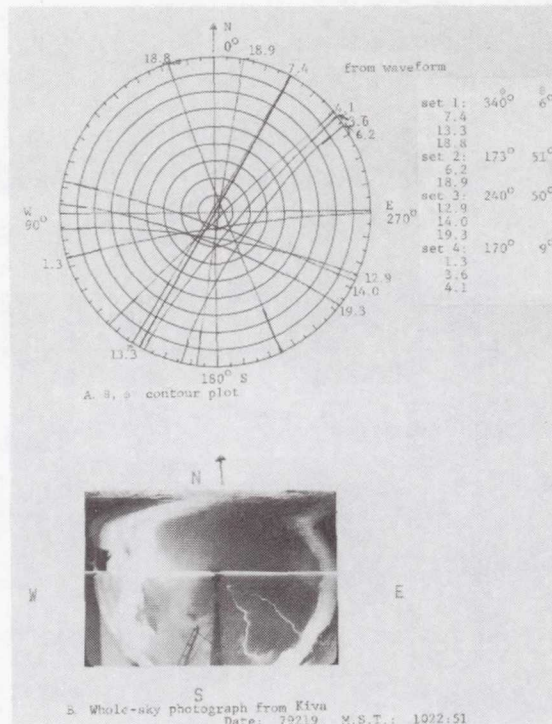
Figure 5.14.- θ, ϕ contours for midrange leader waveform and whole-sky videotape photograph.
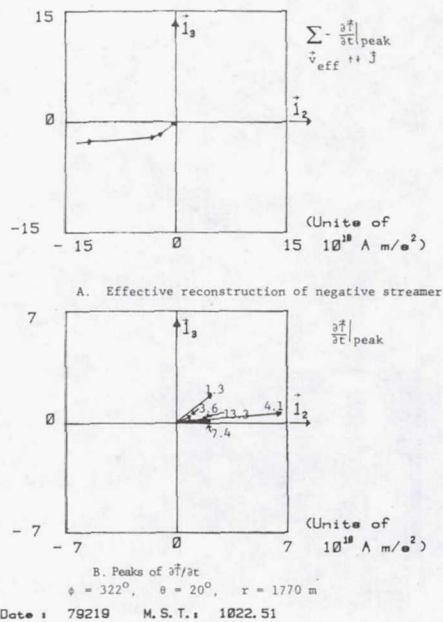
Figure 5.15.- $\partial \vec{T}/\partial t$ for midrange leader (set 1).
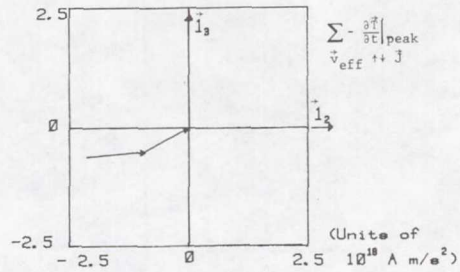
A. Effective reconstruction of negative streamer
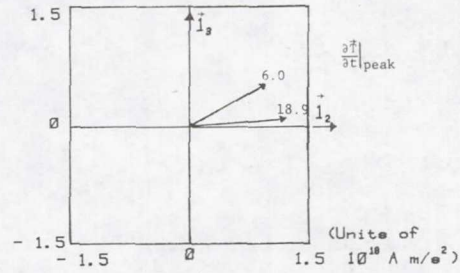
B. Peaks of $\partial\vec{T}/\partial t$

$\phi = 176°,$ $\theta = 36°,$ $r = 681$ m

Date : 79219   M.S.T.: 1022.51

Figure 5.16.- $\partial\vec{T}/\partial t$ for midrange leader (set 2).
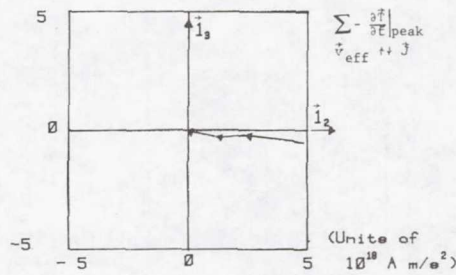
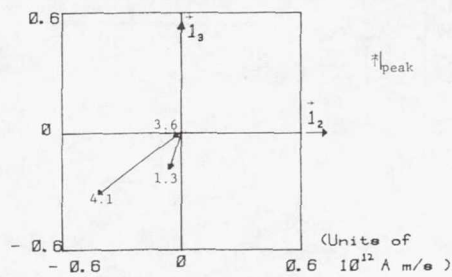A. Effective reconstruction of negative streamer
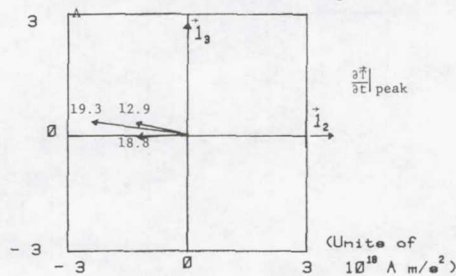
B. Peaks of $\partial\vec{T}/\partial t$

$\phi = 230°,$ $\theta = 67°,$ $r = 435$ m

Date : 79219   M.S.T.: 1022.51

Figure 5.17.- $\partial\vec{T}/\partial t$ for midrange leader (set 3).

1

$\sum - \vec{T}|_{peak}$

$\vec{1}_3$

$\vec{v}_{eff} \leftrightarrow \vec{J}$

0

$\vec{1}_2$

- 1

(Units of

- 1   0   1 10^{12} A m/s)

A. Effective reconstruction of negative streamer

0.3

$\vec{1}_3$

$\vec{T}|_{peak}$

13.3

7.4 $\vec{1}_2$

0

18.8

- 0.3

(Units of

- 0.3   0   0.3 10^{11} A m/s)
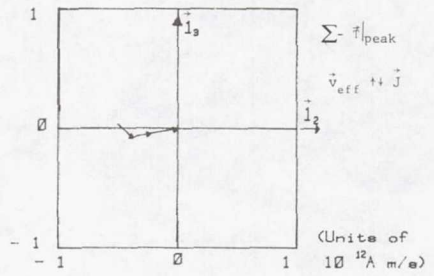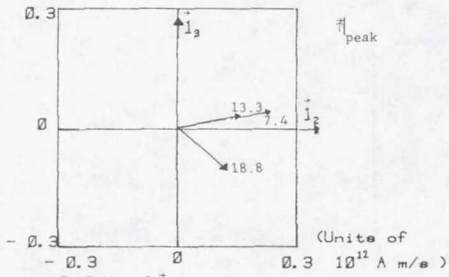
B. Peaks of $\vec{T}$

$\phi = 340^{\circ}$, $\theta = 6^{\circ}$,   r = 3827 m

Date :   79219   M.S.T.:   1022.51

Figure 5.18.- $\vec{T}$ for midrange leader (set 1).

1

$\sum - \vec{T}|_{peak}$

$\vec{1}_3$

$\vec{v}_{eff} \leftrightarrow \vec{J}$

0

$\vec{1}_2$

- 1

(Units of

- 1   0   1 10^{11} A m/s)

A. Effective reconstruction of negative streamer

0.5

$\vec{1}_3$

$\vec{T}|_{peak}$

6.2

18.9 $\vec{1}_2$

0

- 0.5

(Units of

- 0.5   0   0.5 10^{11} A m/s)
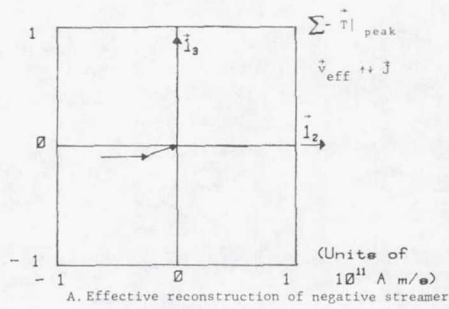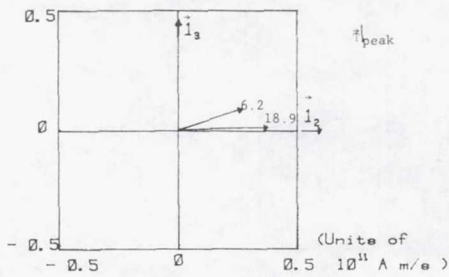
B. Peaks of $\vec{T}$

$\phi = 173^{\circ}$, $\theta = 51^{\circ}$,   r = 515 m

Date :   79219   M.S.T.:   1022.51

Figure 5.19.- $\vec{T}$ for midrange leader (set 2).

72

1.5

$\vec{1}_3$

$\sum - \vec{\tau}|_{peak}$

$\vec{v}_{eff} \leftrightarrow \vec{\jmath}$

∅ $\vec{1}_2$

- 1.5

(Units of

- 1.5   ∅   1.5 10^{11} A m/s)

A.   Effective reconstruction of negative streamer

∅.7

$\vec{1}_3$

$\vec{\tau}|_{peak}$

19.3 12.9
                              $\vec{1}_2$
∅
        14.∅

- ∅.7

(Units of

- ∅.7   ∅   ∅.7 10^{11} A m/s)
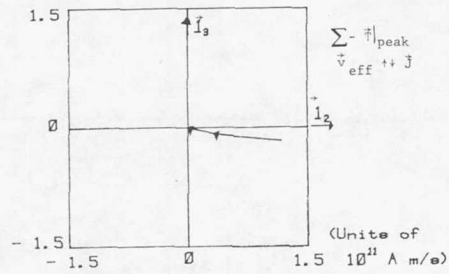
B.   Peaks of $\vec{\tau}$

$\phi = 240°$, $\theta = 50°$,   r = 522 m

Date : 79219   M.S.T.: 1∅22.51

Figure 5.20.- $\vec{T}$ for midrange leader (set 3).

1

$\vec{1}_3$

$\sum - \vec{\tau}|_{peak}$

$\vec{v}_{eff} \leftrightarrow \vec{\jmath}$

∅ $\vec{1}_2$

- 1

(Units of

- 1   ∅   1 10^{12} A m/s)

A.   Effective reconstruction of negative streamer

∅.6

$\vec{1}_3$

$\vec{\tau}|_{peak}$

3.6 $\vec{1}_2$
∅
          1.3

4.1

- ∅.6

(Units of

- ∅.6   ∅   ∅.6 10^{12} A m/s)
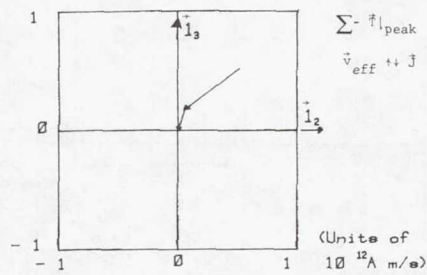
B.   Peaks of $\vec{\tau}$

$\phi = 170°$, $\theta = 9°$,   r ≈ 2557 m

Date : 79219   M.S.T.: 1∅22.51

Figure 5.21.- $\vec{T}$ for midrange leader (set 4).
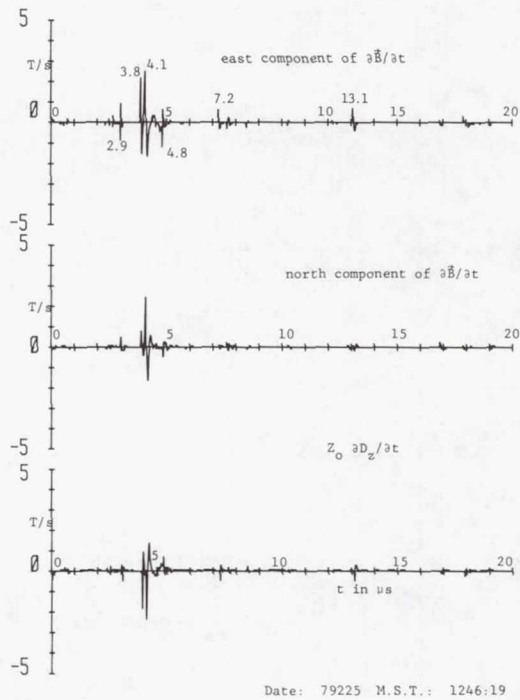
Figure 5.22.- Derivative fields from nearby leader.
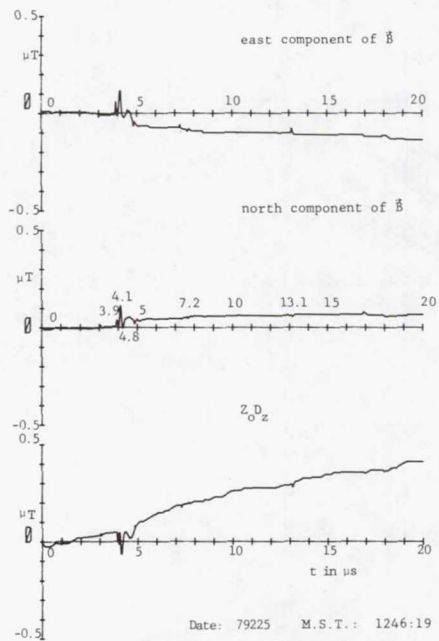
Figure 5.23.- Fields from nearby leader.

Time
code

Thunder
microphone
output

Slow
antenna
$\triangle$E   +

0

-

|← 0.4 seconds →|

$\Delta t = 0.26$ s

horizontal range = 95 m.   HEWLETT

Subsequent strokes

1st return stroke

Stepped
leader
and presumed time of
trigger
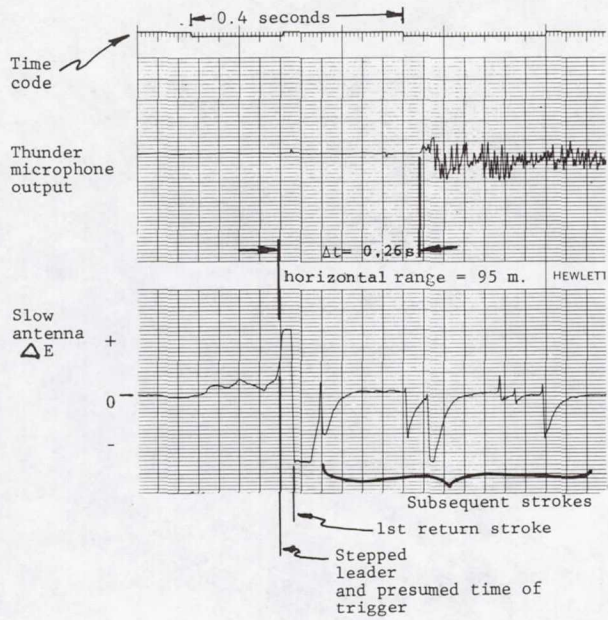
Date: 79225   M.S.T.: 1246:19

Figure 5.24.- Slow electric field change and thunder microphone record
from nearby leader streamer.

ZENITH

$\vec{1}_z$

ESTIMATED
POSITIONS
OF EM SOURCES

NORTH
$\vec{1}_x$

WEST   EAST
$\vec{1}_y$

IRON KIVA

SOUTH   LANGMUIR LAB
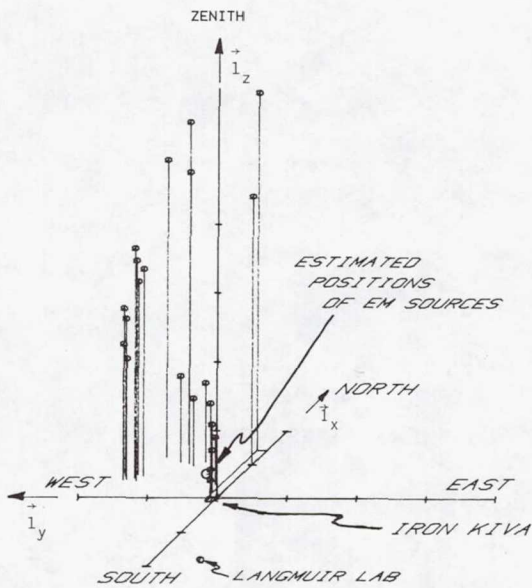
ticks on axes at 1 km intervals

Date :79225   M.S.T. : 1246·19

Figure 5.25.- Acoustic location of lightning with nearby leader streamer.
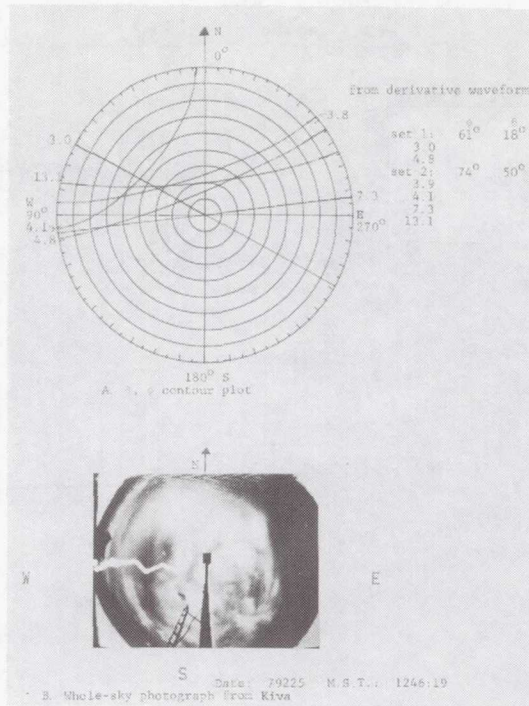
Figure 5.26.- θ,ϕ contours for nearby leader derivative waveform and whole-sky videotape photograph.
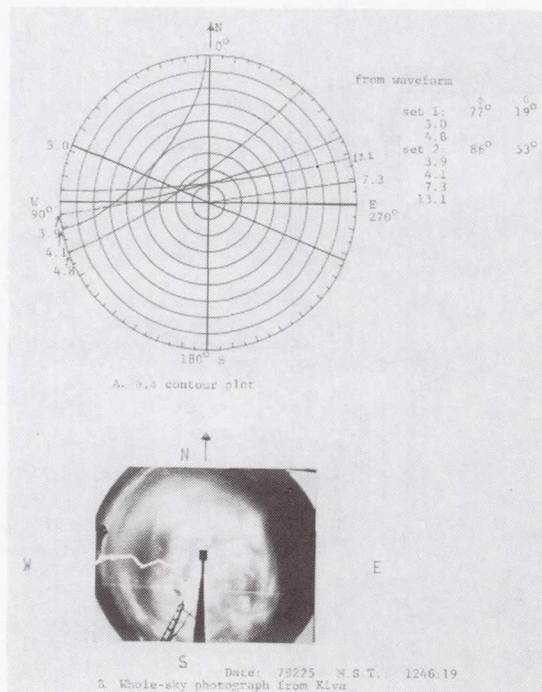
Figure 5.27.- θ,ϕ contours for nearby leader waveform and whole-sky videotape photograph.

Figure 5.28 (top)

1

$\vec{1}_3$

$\sum \frac{\partial \vec{T}}{\partial t}\big|_{peak}$

$\vec{v}_{eff} \uparrow\uparrow \vec{J}$

Ø

$\vec{1}_2$

−1

(Unite of

−1   Ø   1 10^{18} A m/s^2)

A. Effective reconstruction of negative streamer

0.5

$\vec{1}_3$

$\frac{\partial \vec{T}}{\partial t}\big|_{peak}$

Ø

3.0 $\vec{1}_2$

4.8

−0.5

(Unite of

−0.5   Ø   0.5 10^{18} A m/s^2)
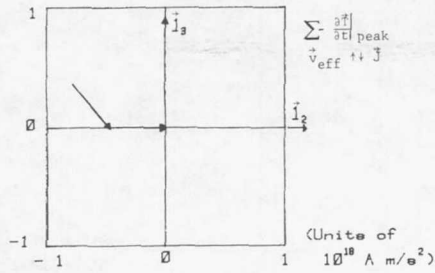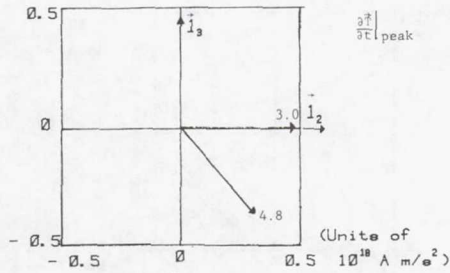
B. Peaks of $\partial \vec{T}/\partial t$

$\phi = 61^\circ$, $\theta = 18^\circ$,   r = 307 m

Date : 79225   M.S.T.: 1246.19

Figure 5.28.- $\vec{\partial T}/\partial t$ for nearby leader (set 1).

Figure 5.29 (bottom)

2

$\vec{1}_3$

$\sum \frac{\partial \vec{T}}{\partial t}\big|_{peak}$

$\vec{v}_{eff} \uparrow\uparrow \vec{J}$

Ø

$\vec{1}_2$

−2

(Unite of

−2   Ø   2 10^{18} A m/s^2)

A. Effective reconstruction of negative streamer

0.7

$\vec{1}_3$

$\frac{\partial \vec{T}}{\partial t}\big|_{peak}$

4.1

3.9

Ø

$\vec{1}_2$

13.1

7.3

−0.7

(Unite of

−0.7   Ø   0.7 10^{18} A m/s^2)
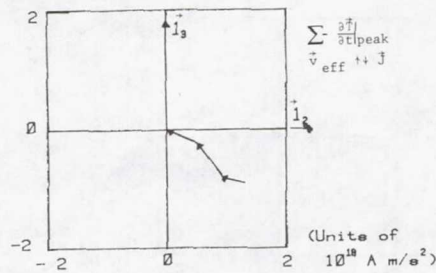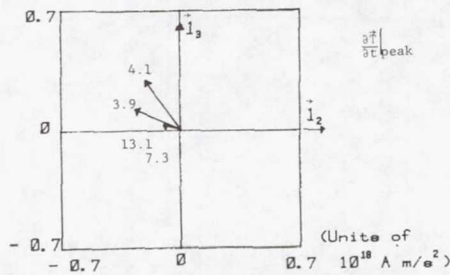
B. Peaks of $\partial \vec{T}/\partial t$

$\phi = 74^\circ$, $\theta = 50^\circ$,   r = 124 m

Date : 79225   M.S.T.: 1246.19

Figure 5.29.- $\vec{\partial T}/\partial t$ for nearby leader (set 2).

77
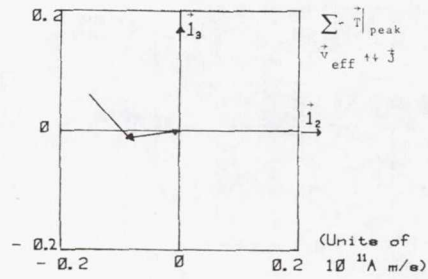
A. Effective reconstruction of negative streamer
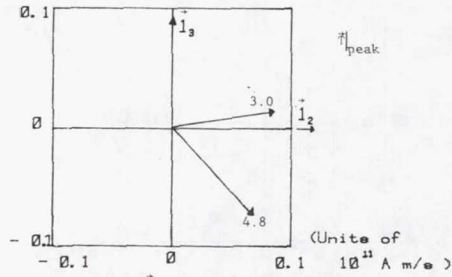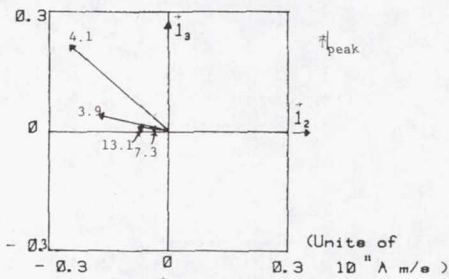

B. Peaks of $\vec{T}$

$\phi = 77^\circ$, $\theta = 19^\circ$, $r = 292$ m

Date: 79225   M.S.T.: 1246.19

Figure 5.30.- $\vec{T}$ for nearby leader (set 1).
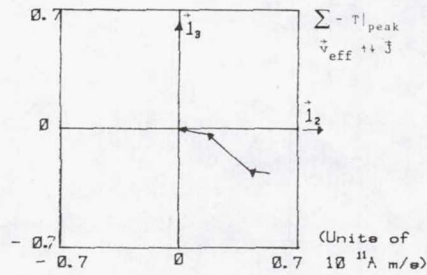
A. Effective reconstruction of negative streamer

B. Peaks of $\vec{T}$

$\phi = 86^\circ$, $\theta = 53^\circ$, $r = 119$ m

Date: 79225   M.S.T.: 1246.19
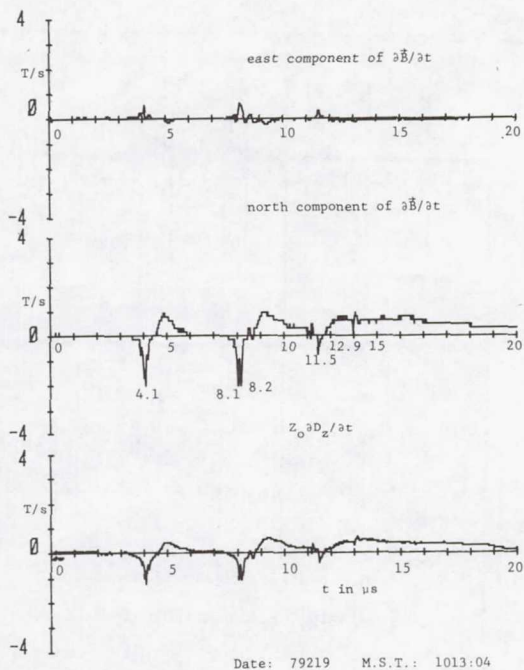
Figure 5.31.- $\vec{T}$ for nearby leader (set 2).

78

east component of $\partial \vec{B}/\partial t$

north component of $\partial \vec{B}/\partial t$

4.1 8.1 8.2 11.5 12.9

$Z_o \partial D_z/\partial t$

t in µs

Date: 79219   M.S.T.: 1013:04

Figure 5.32.- Derivative fields from distant return-stroke.

east component of $\vec{B}$

north component of $\vec{B}$

4.1 8.1 8.2 11.5 12.9

$Z_o D_z$

t in µs

Date: 79219 M.S.T.: 1013:04
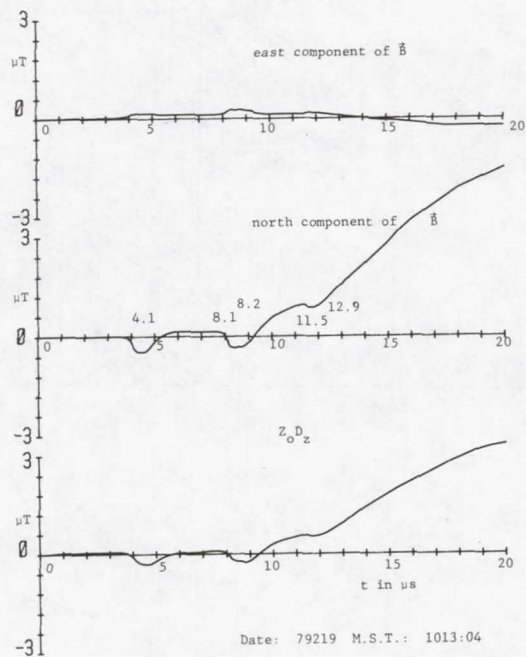
Figure 5.33.- Fields from distant return-stroke.

79
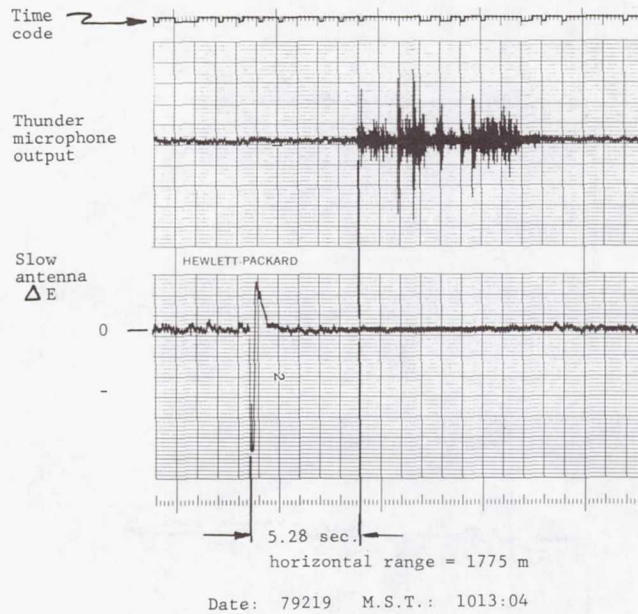
Figure 5.34.- Slow E field change and thunder microphone record
of distant return-stroke.
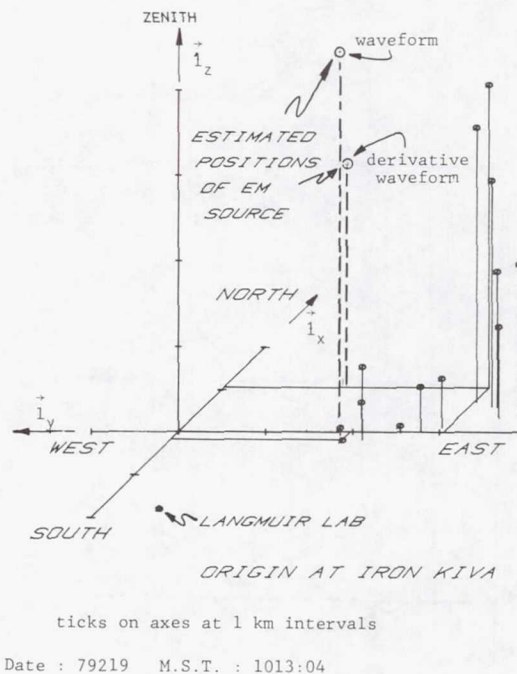
Figure 5.35.- Acoustic location of lightning
with a distant return stroke.
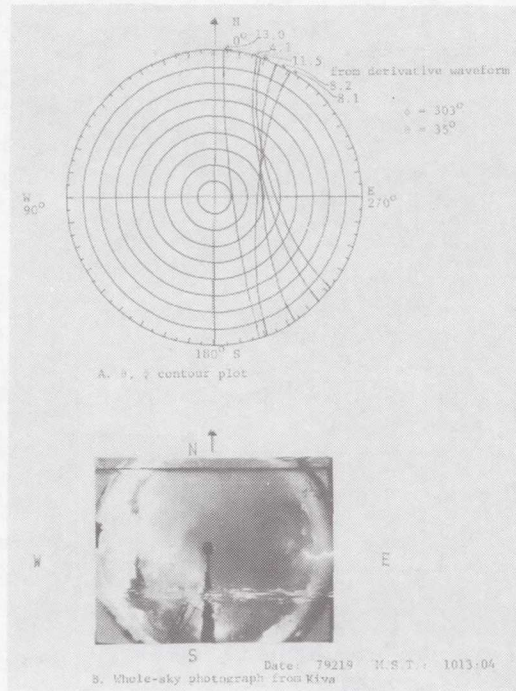
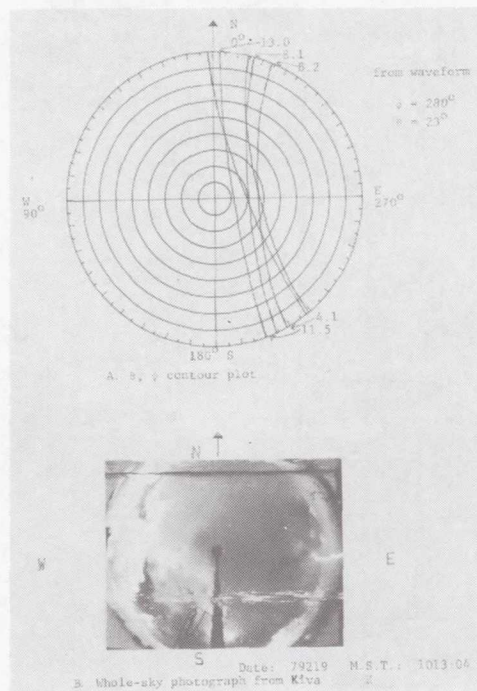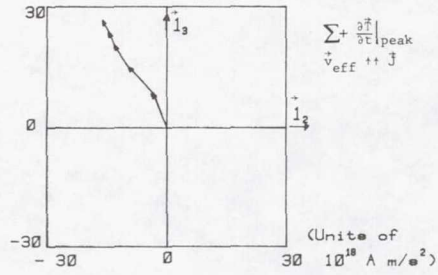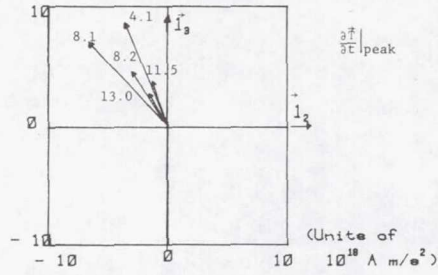Figure 5.36.- θ,φ contours for distant return-stroke derivative waveform and whole-sky videotape photograph.

Figure 5.37.- θ,φ contours for distant return-stroke waveform and whole-sky videotape photograph.
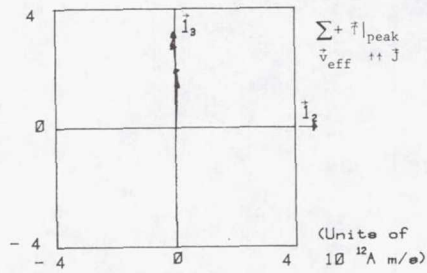
A. Effective reconstruction of positive streamer
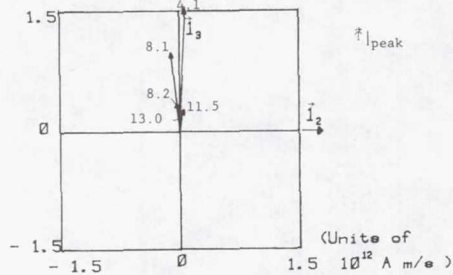
B. Peaks of $\partial \vec{T}/\partial t$

$\phi = 303^{\circ}$, $\theta = 35^{\circ}$, $r = 3138$ m

Date :   79219   M.S.T. :   1013.04

Figure 5.38.- $\partial \vec{T}/\partial t$ for distant return stroke.

A. Effective reconstruction of positive streamer

B. Peaks of $\vec{T}$

$\phi = 280^{\circ}$, $\theta = 23^{\circ}$, $r = 4607$ m

Date :   79219   M.S.T. :   1013.04

Figure 5.39.- $\vec{T}$ for distant return stroke.